

Viscous jetting and Mach stem bifurcation in shock reflections: experiments and simulations

S. S.-M. Lau-Chapdelaine^{1,†}, Q. Xiao¹ and M. I. Radulescu¹

¹Department of Mechanical Engineering, University of Ottawa, 161 Louis Pasteur Pvt., Ottawa, Ontario K1N 6N5, Canada

(Received 20 February 2020; revised 25 June 2020; accepted 26 August 2020)

Shock reflection experiments are performed to study the large-scale convective mixing created by the forward jetting phenomenon. Experiments are performed at a wedge angle of $\theta_w = 30^\circ$ in nitrogen, propane–oxygen and hexane with incident shock Mach numbers up to $M = 4$. Experiments are complemented by shock-resolved viscous simulations of triple-point reflection in hexane for $M = 2.5$ to 6. Inviscid simulations are performed over a wider range of parameters. Reynolds numbers up to $Re \lesssim 10^3$ are covered by simulations and Reynolds numbers of $Re \sim 10^5$ are covered by experiments. The study shows that as the isentropic exponent is lowered, and as the Mach number and Reynolds number are increased, the forward jet approaches the Mach stem, forms a vortex, deforms the shock front and in some cases bifurcates the Mach stem. Experiments show that Kelvin–Helmholtz instabilities in the vortex cause large-scale convective mixing behind the Mach stem at low isentropic exponents ($\gamma \leq 1.15$). The limits of Mach stem bifurcation (triple Mach–White reflection) in inviscid simulations are plotted in the phase space of M – θ_w – γ . A maximum isentropic exponent of $\gamma \approx 1.3$ is found beyond which bifurcation does not occur (at $\theta_w = 30^\circ$). This closely matches the boundary between irregular and regular detonation cellular structures.

Key words: detonation waves, gas dynamics, shock waves

1. Introduction

One major category of shock reflection is the Mach reflection, illustrated in [figure 1](#). It is composed of three shocks: the incident, reflected and Mach shocks, and a slip line joined at the triple point. The slip line separates gas shocked by the incident and reflected shocks from gas shocked by the Mach shock (Mach stem). Under certain conditions ([Hornung 1986](#); [Henderson *et al.* 2003](#)), the slip line curls towards the Mach stem and forms a forward jet. As the isentropic exponent is lowered or the Mach number is increased ([Mach 2011](#)), the head of the forward jet approaches the Mach stem, eventually causing it to bulge, kink or even bifurcate, meaning a new triple point is formed on the Mach stem. The jet rolls up into a large vortex behind the Mach stem.

[†] Present address: Department of Chemistry and Chemical Engineering, Royal Military College, 11 Crerar Crescent, Kingston, Ontario K7K 7B4, Canada. Email address for correspondence: shem.lau-chapdelaine@rmc.ca

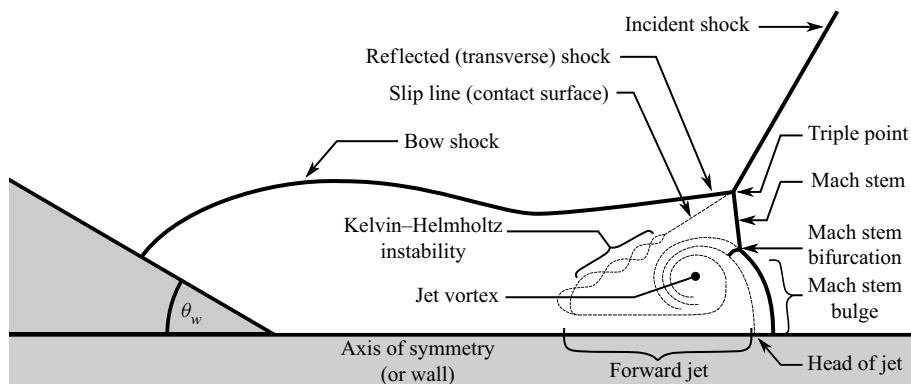


FIGURE 1. Illustration of a Mach reflection with Mach stem bifurcation.

The configuration of shock reflection depends on three parameters: the Mach number M , angle of reflection (i.e. wedge angle θ_w) and the isentropic exponent (heat capacity ratio) γ . Classifications of shock reflection types are presented in the works of

Ben-Dor (2007), Vasilev, Elperin & Ben-Dor (2008) and Semenov, Berezkina & Krassovskaya (2012) and thorough reviews on shock reflections have been written by Hornung (1986) and Ben-Dor (2007).

The parameters that lead to forward jet and vortex formation are typical of hydrocarbon detonations (i.e. low γ , high M). These phenomena are important to understanding the multidimensional instability and propagation limits of detonations. For instance, the forward jet (Sorin *et al.* 2009) and vortex are believed to accelerate reaction rates through large-scale mixing (Maley *et al.* 2015), while Mach stem bifurcation caused by the jet is postulated (Radulescu *et al.* 2009) to be a source of new detonation cells.

In this study, inert shock reflection simulations and experiments are used to investigate the cause of large-scale mixing in shock reflections as they pertain to detonations. Particular attention will be placed on the role of the forward jet and the jet–shock interaction. The simulations and experiments are designed to overcome some of the challenges posed by traditional wedge reflection configurations.

There is conflicting evidence on the prominence of the jet and vortex, or the conditions under which they affect the shape of the shock front. Comparisons of experiments and inviscid simulations (Glaz *et al.* 1985*a,b*) have found that the Mach stem bulges more in simulations than experiments. Bulging can become severe enough to cause Mach stem bifurcation in inviscid simulations (e.g. Mach 2011) but has only been observed in a few experiments (Semenov, Berezkina & Krasovskaya 2009*b*; Mach & Radulescu 2011; Maley *et al.* 2015).

The fundamental issue with the Euler equations, often used to model shock reflections and detonations, is that they do not converge in multidimensional cases featuring slip lines (Samtaney & Pullin 1996). The shock reflection and forward jet behave differently depending on the numerical scheme and grid layout (Quirk 1992; Lau-Chapdelaine & Radulescu 2013) as they differ in how artificial diffusion is introduced. The shortcomings of the Euler equations are overcome in this study by use of the Navier–Stokes equations.

Implementation of the reflecting surface also poses problems. In simulations, surfaces oblique to the grid alter the reflection configuration depending on how they are implemented (Ben-Dor *et al.* 1987; Lau-Chapdelaine & Radulescu 2013). This will be avoided by using triple-point reflections (Lau-Chapdelaine & Radulescu 2016) from grid-aligned surfaces.

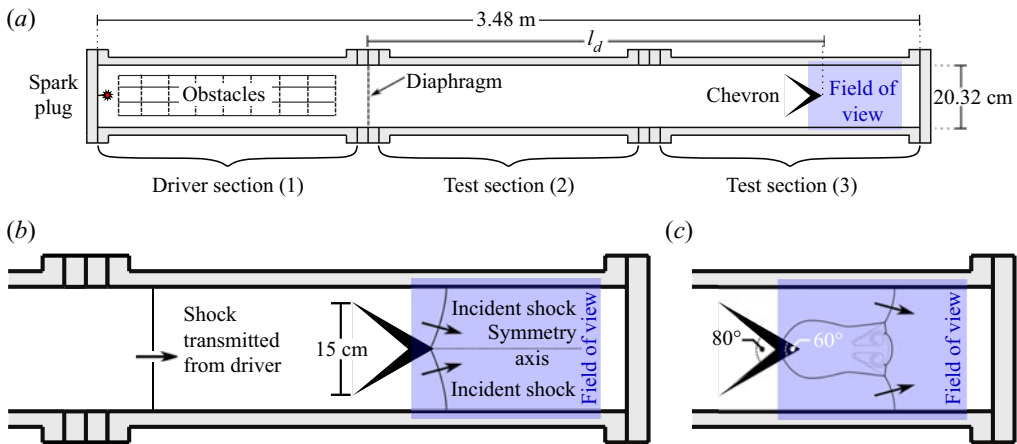


FIGURE 2. Diagram of the shock tube with a depth of 1.91 cm; optical access throughout the third section; the chevron had an 80° inner apex, 60° outer apex, 15 cm outside edges. (a) Apparatus. (b) Transmitted and incident shocks in the test section, (c) Subsequent shock reflection.

Boundary layers on the reflecting surface change the effective wedge angle (Hornung 1985; Ben-Dor 2007) and cause the forward jet to oscillate (Vasilev *et al.* 2004; Shi *et al.* 2017). While most simulations use free-slip boundaries, the few experiments (Smith 1959; Henderson & Lozzi 1975; Higashino, Henderson & Shimizu 1991; Barbosa & Skews 2002) performed with free-slip surfaces were focused on the transition from regular to irregular reflection. Shock reflections in detonations happen on a symmetry boundary, where boundary layers are absent, and there is a need for experiments to explore jetting under these conditions.

In this study, well-posed experiments and simulations are used to explore the conditions that lead to a strong forward jet, vortex and jet–shock interaction. This is done through experiments of shock reflection from a plane of symmetry, shock-resolved Navier–Stokes simulations and inviscid simulations. Viscous simulations are performed at Reynolds numbers up to $Re \sim 10^3$ and experiments up to $\sim 10^5$. For comparison, detonations in stoichiometric hydrogen–oxygen, methane–oxygen and propane–oxygen under atmospheric conditions have been estimated to reach Reynolds numbers of $\sim 10^5$ to 10^6 on cellular length scales (Lau-Chapdelaine & Radulescu 2016). The effects of Reynolds number, Mach number and isentropic exponent on the forward jet, the flow field behind the Mach stem and the shock front are scrutinized. Conditions where jet–shock interactions become important are determined and their boundaries are reported.

The experiments are addressed in § 2 followed by numerical simulations in § 3. The discussion is found in § 4 and the conclusion in § 5.

2. Experiments

2.1. Experimental technique

Experiments were carried out in a detonation-driven aluminium shock tube illustrated in figure 2(a) and described by Maley (2015). The shock tube measured 3.48 m in length and had a rectangular cross-section measuring 20.32 cm tall by 1.91 cm in depth. A diaphragm separated the driver and test sections.

Experiment	Test mixture	\hat{T}_0 (°C)	\hat{p}_0 (kPa)	\hat{l}_d (m)	$\hat{\lambda}_0$ (μm)	γ_0	M_c	Figures	Movie
1	N ₂	20.5	3.7	1.85	1.8	1.40	2.4	3(a) to 3(c)	1
2	N ₂	19.0	3.4	1.85	1.9	1.40	3.0	3(d) to 3(f)	2
3	N ₂	20.5	3.8	1.85	1.7	1.40	3.5	3(g) to 3(i)	3
4	0.8C ₃ H ₈ + 0.2O ₂	21.0	6.96	1.85	0.407	1.15	2.4	4(a) to 4(c)	4
5	0.8C ₃ H ₈ + 0.2O ₂	22.0	3.5	1.85	0.81	1.15	2.9	4(d) to 4(f)	5
6	0.8C ₃ H ₈ + 0.2O ₂	21.5	3.9	1.85	0.74	1.15	3.5	4(g) to 4(i)	6
7	C ₆ H ₁₄	20.0	2.6	1.85	0.51	1.06	2.5	5(a) to 5(c)	7
8	C ₆ H ₁₄	22.5	2.6	1.85	0.52	1.06	2.7	5(d) to 5(f)	8
9	C ₆ H ₁₄	23.0	2.3	1.85	0.56	1.06	3.4	5(g) to 5(i)	9
10	0.8C ₃ H ₈ + 0.2O ₂	23.0	14.3	0.32	0.199	1.15	4.0	6(a) to 6(c)	10
11	C ₆ H ₁₄	23.5	~3.5	0.68	0.38	1.06	4.0	6(d) to 6(f)	11

TABLE 1. Experimental conditions.

The shock tube was evacuated to $\lesssim 80$ Pa before gases were introduced. The driver section was filled with stoichiometric ethylene–oxygen (C₂H₄ + 3O₂). The test section was filled with a gas selected for its isentropic exponent, listed in table 1. Nitrogen was used for $\gamma_0 = 1.4$, an inert rich-propane–oxygen mixture (0.8C₃H₈ + 0.2O₂) for $\gamma_0 = 1.15$ and normal hexane for $\gamma_0 = 1.06$. The subscript 0 refers to the unshocked state.

Experiments were initiated with a spark that ignited the driver gas. A mesh of obstacles in the first third of the shock tube promoted detonation initiation in the driver section. The detonation ruptured the diaphragm, transmitting a shock into the test section.

The diaphragm was composed of aluminium foil covered by aluminium tape on the test gas side. An ‘I’-shaped slot matching the channel dimensions was cut through the tape. The foil separated the driver and test gases and opened along the slot in the tape when hit by the detonation. The tape kept the foil in place during opening, preventing diaphragm petals from polluting the test section with large fragments, though small fragments still formed. Experiment 10 used a plastic sheet as a diaphragm (an exception, from the diaphragm selection process).

The transmitted shock travelled through the test gas to a chevron-shaped obstacle. The top and bottom portions of the shock diffracted past the chevron (figure 2b) and reflected from each other at the trailing edge (figure 2c). The chevron tip was located in the last third of the shock tube at a distance \hat{l}_d from the diaphragm, listed in table 1. The chevron limbs measured 15 cm on the outside and had a 60° outer apex. This made for reflection with a wedge angle of $\theta_w = 30^\circ$. The geometry was chosen to approximate the angle between shocks at the end of a detonation cell (Strehlow & Biller 1969; Austin 2003; Radulescu *et al.* 2009; Bhattacharjee 2013).

Glass walls on the last third of the shock tube allowed optical access. A Z-type schlieren with a vertical knife edge was used to capture high-speed movies with a Phantom v1210 camera at 77 481 frames per second with 0.468 μs exposures and a resolution of 384 × 288 pixels. The movies were centred downstream of the chevron with the trailing edge in view.

The strength of the shock interacting with the obstacle was controlled by the pressure ratio between driver and test gases. It was also affected by the distance between the diaphragm and chevron, and the diaphragm construction. Higher pressure ratios, shorter separation distances and fewer layers of tape made for stronger shock waves.

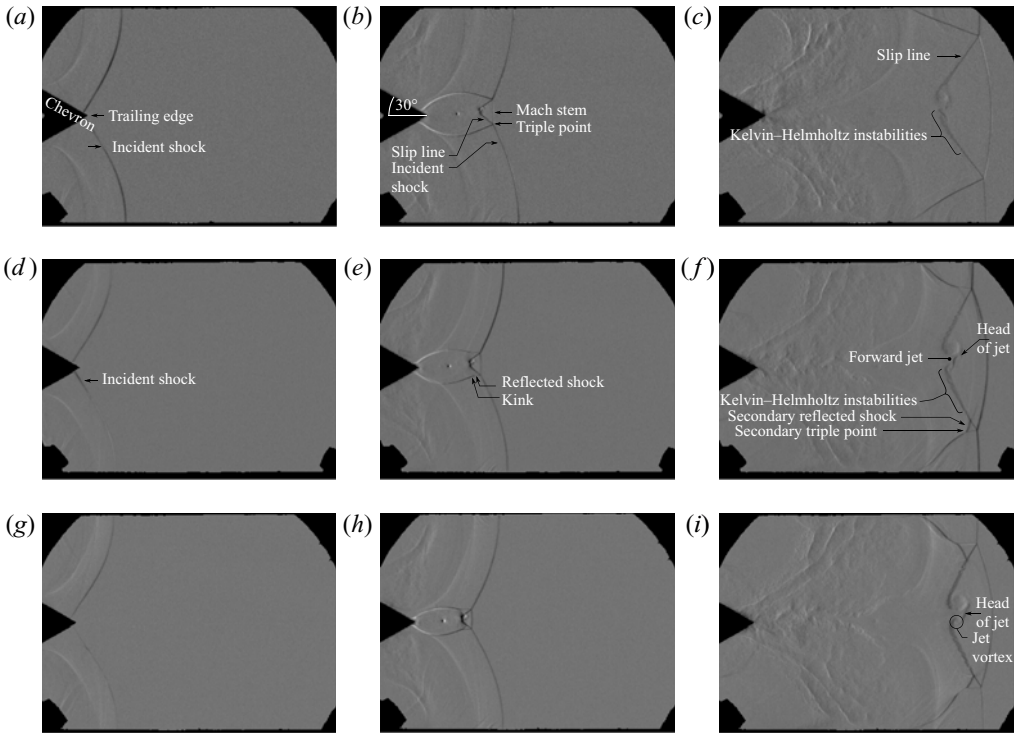


FIGURE 3. Schlieren photographs of nitrogen experiments ($\gamma_0 = 1.4$, $\theta_w = 30^\circ$): (a) $M_c = 2.4$; (b) $Re = 1.9 \times 10^4$, $\hat{t} = 64.5 \mu\text{s}$; (c) $Re = 1.1 \times 10^5$, $\hat{t} = 232 \mu\text{s}$; (d) $M_c = 3.0$; (e) $Re = 2.3 \times 10^4$, $\hat{t} = 51.6 \mu\text{s}$; (f) $Re = 1.5 \times 10^5$, $\hat{t} = 194 \mu\text{s}$; (g) $M_c = 3.5$; (h) $Re = 2.5 \times 10^4$, $\hat{t} = 38.7 \mu\text{s}$; (i) $Re = 1.9 \times 10^5$, $\hat{t} = 168 \mu\text{s}$.

2.2. Experimental results

Experimental results are shown in figures 3, 4 and 5. They are a sample of the experiments performed. Movies are supplied as supplementary movies available at <https://doi.org/10.1017/jfm.2020.731>.

Each row of the figures shows three snapshots from one experiment. The first frame is taken immediately before reflection, and the two subsequent frames are taken from later times. The Mach number M_c noted in the figures is the shock strength on the chevron surface prior to reflection, calculated using the averaged shock spacing between frames, the inter-frame delay and sound speed of the unshocked gas. The channel height of 0.2032 m is used to scale the photographs. Each row corresponds to a different experiment.

The schlieren photographs show horizontal density gradients. Bright features indicate an increase of density from left to right, and vice versa.

2.2.1. Experiments in nitrogen ($\gamma_0 = 1.4$)

Figure 3(a) shows a schlieren photograph of an experiment in nitrogen gas, $\gamma_0 = 1.4$, immediately before shock reflection. The dark curves are two shocks that have diffracted over the obstacle, travelling to the right at $M_c = 2.4$. These form the incident shocks for the reflection in the following frames. The asymmetry in shock strengths prior to reflection was typically below 5% of M_c . The flow field is shown 64.5 μs later in figure 3(b).

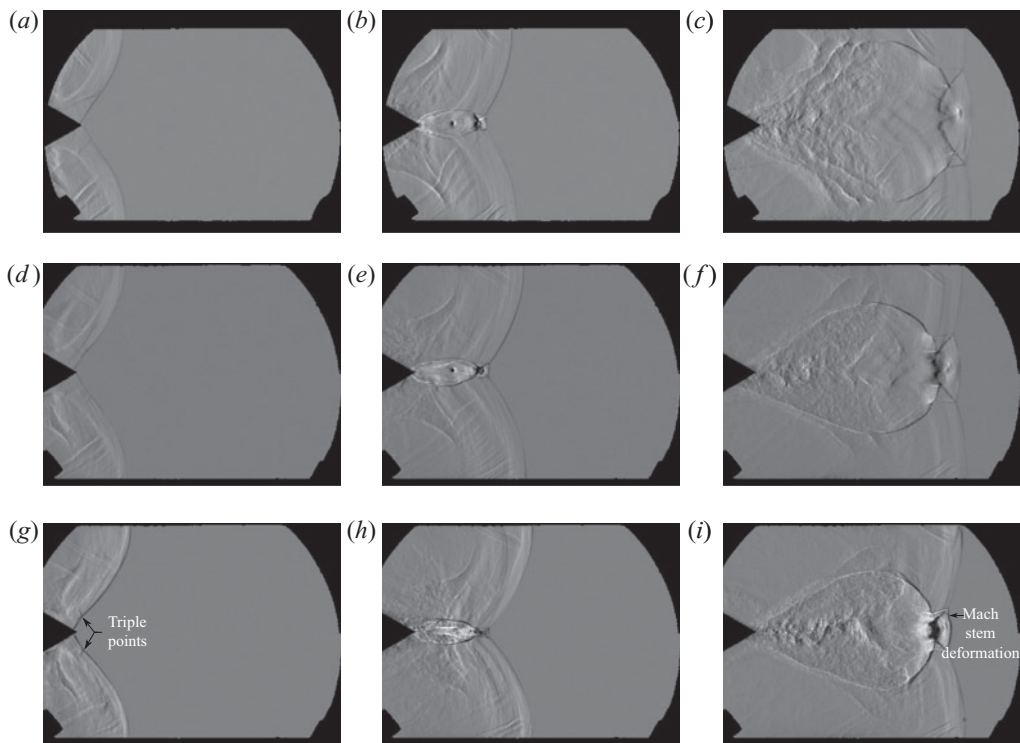


FIGURE 4. Schlieren photographs of propane–oxygen experiments ($\gamma_0 = 1.15$, $\theta_w = 30^\circ$): (a) $M_c = 2.4$; (b) $Re = 1.2 \times 10^5$, $\hat{t} = 90.3 \mu\text{s}$; (c) $Re = 7.3 \times 10^5$, $\hat{t} = 310 \mu\text{s}$; (d) $M_c = 2.9$; (e) $Re = 7.9 \times 10^4$, $\hat{t} = 77.4 \mu\text{s}$; (f) $Re = 3.7 \times 10^5$, $\hat{t} = 219 \mu\text{s}$; (g) $M_c = 3.5$; (h) $Re = 7.9 \times 10^4$, $\hat{t} = 64.5 \mu\text{s}$; (i) $Re = 3.8 \times 10^5$, $\hat{t} = 168 \mu\text{s}$.

Single Mach reflections are formed with a nearly straight Mach stem. Slip lines emanate from the triple points and curl towards the Mach stem near the axis of symmetry. The flow field 232 μs after reflection is shown in figure 3(c). The Mach stem has grown to occupy most of the channel and has curved due to unsteadiness. Kelvin–Helmholtz instabilities have appeared along the slip lines.

The Mach number is increased to $M_c = 3.0$ in the next experiment by increasing the pressure ratio between driver and test gas. A transitional Mach reflection is formed (figure 3e) and transitions to a double Mach reflection (figure 3f), seen by the formation of a secondary triple point and reflected shock where there was previously a kink. The slip line curls into a forward jet that is longer and closer to the Mach stem than before.

A double Mach reflection is formed (figure 3h) in the next experiment, at $M_c = 3.5$, and vortices begin to form at the head of the jet (figure 3i).

2.2.2. Experiments in propane with oxygen ($\gamma_0 = 1.15$)

The set of experiments in figure 4 are performed for the same Mach numbers but with a lower isentropic exponent of $\gamma_0 = 1.15$, by changing the test gas to rich-propane–oxygen. Double Mach reflections are seen in all cases.

At $M_c = 2.4$ (figure 4b), the slip lines curl forward into a forward jet (figure 4c) that is more distinct and closer to the Mach stem than of all the $\gamma_0 = 1.4$ cases. The jet terminates with a vortex. Kelvin–Helmholtz instabilities on the slip line are entrained into the jet.

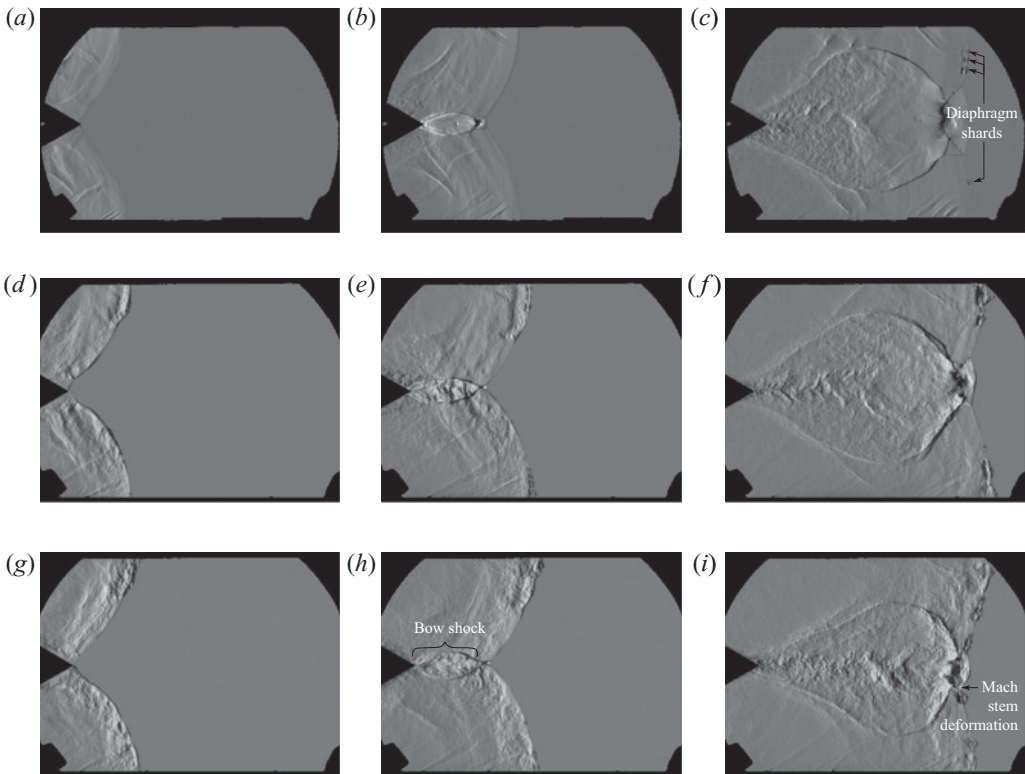


FIGURE 5. Schlieren photographs of hexane experiments ($\gamma_0 = 1.06$, $\theta_w = 30^\circ$): (a) $M_c = 2.5$; (b) $Re = 1.1 \times 10^5$, $\hat{t} = 129 \mu\text{s}$; (c) $Re = 6.8 \times 10^5$, $\hat{t} = 426 \mu\text{s}$; (d) $M_c = 2.7$; (e) $Re = 5.1 \times 10^4$, $\hat{t} = 103 \mu\text{s}$; (f) $Re = 5.2 \times 10^5$, $\hat{t} = 323 \mu\text{s}$; (g) $M_c = 3.4$; (h) $Re = 1.0 \times 10^5$, $\hat{t} = 90.3 \mu\text{s}$; (i) $Re = 7.5 \times 10^5$, $\hat{t} = 258 \mu\text{s}$.

At $M_c = 2.9$ (figure 4e), the vortex at the head of the forward jet (figure 4f) has a rough appearance caused by the entrainment of Kelvin–Helmholtz instabilities which create a turbulent substructure.

Increasing the Mach number to $M_c = 3.5$ causes triple points to form on the diffracting shocks (figure 4g). These triple points are a result of the diffraction process (Skews 1967). After reflection (figure 4i), the forward jet impinges on the Mach stem, causing it to deform, bulge along the centre line and possibly bifurcate. A large portion of the region behind the Mach stem has a turbulent appearance.

2.2.3. Experiments in hexane ($\gamma_0 = 1.06$)

The isentropic exponent was lowered to $\gamma_0 = 1.06$ by employing *n*-hexane as the test gas. The double Mach reflection formed at $M_c = 2.5$ (figure 5c) is qualitatively similar to the $M_c = 2.9$, $\gamma_0 = 1.15$ case (figure 4f). Kelvin–Helmholtz instabilities appear close to the triple point and are entrained into the jet vortex, giving it a turbulent appearance that is distinct from the rest of the comparatively smooth-looking region behind the Mach stem. This rough, turbulent appearance of the vortex is present in all experiments where $M_c \geq 2.5$ and $\gamma_0 = 1.06$.

The four triangular protrusions from the incident shocks seen in figure 5(c) are small diaphragm shards that have overtaken the shock. This occurs because the highly

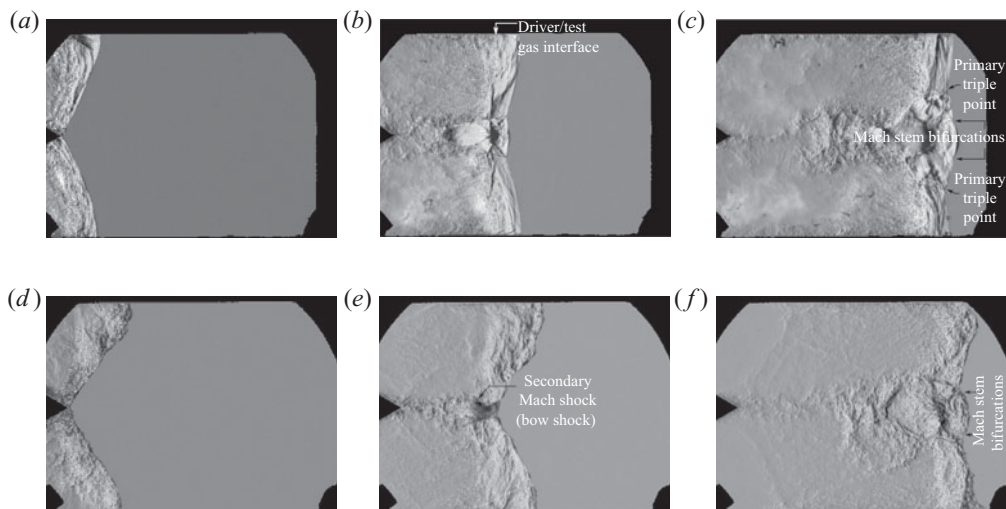


FIGURE 6. Schlieren photographs of experiments at a larger Mach number ($M_c = 4.0$, $\theta_w = 30^\circ$; (a–c): propane–oxygen; (d–f): hexane): (a) $\gamma_0 = 1.15$; (b) $Re = 2.2 \times 10^6$, $\hat{t} = 103 \mu\text{s}$; (c) $Re = 4.7 \times 10^6$, $\hat{t} = 219 \mu\text{s}$; (d) $\gamma_0 = 1.06$; (e) $Re = 5.8 \times 10^5$, $\hat{t} = 103 \mu\text{s}$; (f) $Re = 2.3 \times 10^6$, $\hat{t} = 258 \mu\text{s}$.

compressible (low isentropic exponent) layer of gas between the shock and driver–test gas interface is thinner than in the other gases, which allows spall from the diaphragm to catch up to the shock front.

The Mach stem becomes shorter when the Mach number is increased to $M_c = 2.7$, making it difficult to see the flow field behind the shock front at early times (figure 5e). A forward jet that impinges on the Mach stem becomes visible as the reflection grows (figure 5f). The forward jet in the following experiment, $M_c = 3.4$, reaches the Mach stem and causes it to deform and possibly bifurcate (figure 5i).

The schlieren photographs in the last two cases (figure 5d–i) have a textured appearance behind the Mach stem, incident and reflected shocks that is absent from the comparably smooth-looking flow fields seen all the previous cases, vortex aside. The textured appearance makes it difficult to observe fine features and suggests there is a flow instability present. This instability is not caused by the presence of driver gas, is discussed in §§ 2.2.4 and 4.4 and the appendix.

2.2.4. Experiments at a larger Mach number

In order to increase the Mach number further, the distance between the diaphragm and the chevron had to be shortened. The results are shown in figure 6.

In both gases, double Mach reflections are formed with Mach stems that are taller than expected from the previous cases. This is due to the influence of the driver–test gas interface. The forward jets reach the Mach stem and cause them to curve and bifurcate, seen in the last column of figure 6.

Moving the diaphragm too close to the chevron causes the driver gas to interfere with the reflection. All of the previous experiments (figures 3 to 5) are not affected by the presence of the driver gas. This is evidenced by the fact that their bow shocks (i.e. the horizontal reflected shocks between the triple point and chevron, see figure 5h) remain intact and attached to the chevron. These shocks are absent in figure 6 where contamination by the

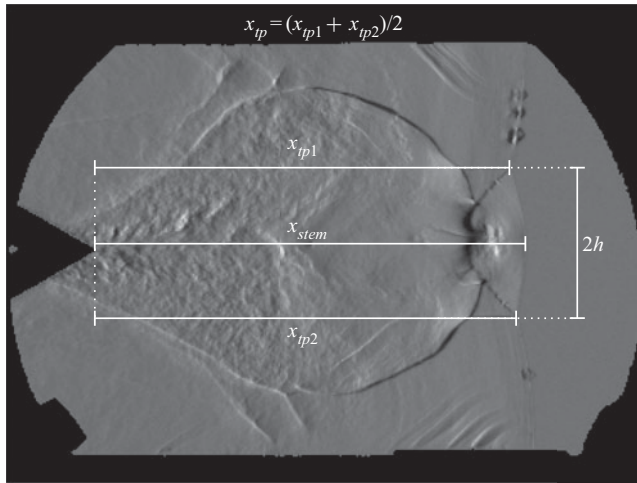


FIGURE 7. Definitions of x_{tp} , x_{stem} and h .

high-sound-speed driver gas causes them to disperse. Simulations in the [appendix](#) support that the driver–test gas interface is far from the leading shock in the previous experiments.

2.2.5. Summary of experimental results

A series of experiments were performed with $Re \sim 10^5$ to 10^6 , $M_c = 2.4$ to 4 and $\gamma_0 = 1.4$ to 1.06 . The experiments show that decreasing the isentropic exponent and increasing the Mach number cause a transition from single Mach reflection, to transitional Mach reflection, onto double Mach reflection. The forward jet and vortex gradually become stronger and eventually deform the Mach stem as the isentropic exponent decreases and the Mach number is increased. Concurrently, Kelvin–Helmholtz instabilities become entrained in the vortex, resulting in a turbulent structure behind the Mach stem in the cases with lower isentropic exponents.

2.2.6. Mach stem bulging

The size or ‘strength’ of the forward jet and vortex is difficult to measure at moderate Mach numbers ($\gtrsim 3$) and low isentropic exponents (≤ 1.15) due to the short Mach stems and the rough appearance of the photos behind the shock front. The bulging of the Mach stem foot is measured instead, as a proxy of the jet’s strength. Bulging is measured as the horizontal distance between the rightmost point of the Mach stem (x_{stem}) and the triple point (x_{tp} , averaged between the top and bottom triple points), and normalized by the Mach stem height h (see [figure 7](#)). Bulging, $(x_{stem} - x_{tp})/h$, is plotted against the Reynolds number in [figure 8](#). Each point corresponds to one frame from the movies.

The Reynolds number for a Mach reflection was defined as

$$Re = \frac{u_{shear}}{v_{mean}} h \tag{2.1}$$

by Rikanati *et al.* (2006, 2009) to study Kelvin–Helmholtz instability along the slip line. Here u_{shear} is the velocity difference across the slip line and v_{mean} is the kinematic viscosity averaged across the slip line. This definition takes into account the velocity and viscosity across the slip line (which forms the forward jet) where diffusion is expected to be

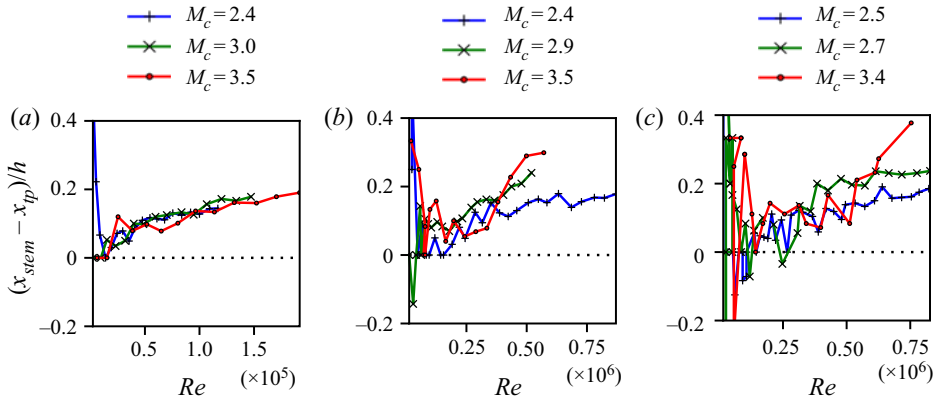


FIGURE 8. Evolution of the Mach stem bulging in experiments: (a) $\gamma_0 = 1.4$; (b) $\gamma_0 = 1.15$; (c) $\gamma_0 = 1.06$.

γ_0	1.4			1.15				1.06			
M_c	2.4	3.0	3.5	2.4	2.9	3.5	4.0	2.5	2.7	3.4	4.0
Re/\hat{h} (mm ⁻¹)	1602	2138	2797	14 490	11 171	17 635	79 818	18 523	22 926	38 219	78 506

TABLE 2. Estimate of Reynolds number growth rates.

important, and the Mach stem height h provides an easily measured characteristic length scale.

Three shock theory is used to get analytical estimates of the shear velocity and viscosity, which are assumed constant. The inputs required for the calculation are the wedge angle $\theta_w = 30^\circ$, isentropic exponent γ_0 , incident shock strength M_c and the unshocked temperature and pressure listed in table 1. The estimates for $\hat{u}_{shear}/\hat{v}_{mean} = Re/\hat{h}$ are listed in table 2, giving Reynolds numbers as a function of Mach stem height. The Mach stem height is measured directly from experiments as half the vertical distance between triple points. For example, the distance between triple points in figure 3(b) is $2\hat{h} = 24$ mm, and $Re/\hat{h} = 1602$ mm⁻¹ (table 2), yielding a Reynolds number of $Re = 19\,000$.

In a self-similar pseudo-steady reflection, Mach stem bulging would draw a horizontal line in figure 8. However, the incident shocks are curved in these experiments, causing the reflection angle and shock strength to change continuously, leading to more bulging as Reynolds number increases.

Bulging is approximately equal in all gases at $M_c \approx 2.5$ and is independent of Mach number in the $\gamma_0 = 1.4$ experiments because the jet never reaches the shock front. The additional bulging in the $\gamma_0 = 1.15$ and $\gamma_0 = 1.06$ gases at higher Mach numbers is caused when the forward jet approaches or contacts the Mach stem. Jetting becomes strong enough to cause bulging when the isentropic exponent is sufficiently low ($\gamma_0 \leq 1.15$) and the Mach number is sufficiently large ($M_c \gtrsim 3$). The vortex is turbulent in these cases.

3. Numerical prediction

The experiments were limited to moderate Mach numbers and large Reynolds numbers. Numerical simulations will now be used to elucidate the flow field at early stages of the

reflection and at higher Mach numbers. The numerical study is an extension of the work by Lau-Chapdelaine & Radulescu (2016).

3.1. Numerical technique

The two-dimensional, laminar, unsteady Navier–Stokes equations for a calorically perfect gas were used. A Prandtl number of 3/4 was used for all the simulations and the isentropic exponent was uniform throughout the domain. Bulk viscosity was neglected, and viscosity and heat conductivity were assumed to be power laws of temperature and a known reference state:

$$\hat{\mu} = \hat{\mu}_{ref} \sqrt{\frac{\hat{T}}{\hat{T}_{ref}}} \quad \text{and} \quad \hat{k} = \hat{k}_{ref} \sqrt{\frac{\hat{T}}{\hat{T}_{ref}}}. \tag{3.1a,b}$$

The equations were non-dimensionalized using the unshocked gas (subscript 0) as reference state (subscript ‘ref’):

$$\hat{\rho}_{ref} = \hat{\rho}_0, \quad \hat{p}_{ref} = \hat{p}_0, \quad \hat{T}_{ref} = \hat{T}_0, \quad \hat{x}_{ref} = \hat{\lambda}_0 = \frac{\hat{\mu}_0}{\hat{p}_0} \sqrt{\frac{\pi \hat{R}_s \hat{T}_0}{2}}, \tag{3.2a-d}$$

where ρ is density, p is pressure, T is temperature, x is the spatial dimension, R_s is the specific gas constant and the circumflex (hat) indicates dimensional variables. The spatial dimension was non-dimensionalized by the mean free path in the unshocked gas $\hat{\lambda}_0$, listed in table 1 for the experimental conditions, and time was non-dimensionalized by $\hat{t}_{ref} = \hat{\lambda}_0 \sqrt{\hat{\rho}_0 / \hat{p}_0}$ for consistency.

The Navier–Stokes equations are valid in the continuum regime (Knudsen number $Kn = \lambda/L < 0.01$, where L is a characteristic length scale), and in the slip flow regime ($0.01 < Kn < 0.1$), where special conditions are required near walls (Faghri & Zhang 2006). Because shock reflection from a symmetry condition is studied instead of reflection from a wall, the Navier–Stokes equations remain valid in the slip flow regime. The simulations that are presented in the next section (figure 12, at $Re \approx 1000$) have Knudsen numbers of $\lambda_0/h = 0.009$ to 0.06 in the unshocked gas and $\lambda_M/h = 0.001$ to 0.003 behind the Mach shock, where the slip line and forward jet lie, which are well within the validity range of the Navier–Stokes equations.

The equations were solved using the *mg* software package developed by Falle (Falle 1991; Falle & Komissarov 1996). A second-order Godunov scheme using a monotonized central symmetric flux limiter (Van Leer 1977) solved convective terms, and diffusion was solved explicitly in time with second-order central differences in space.

A Cartesian grid with adaptive mesh refinement (Sharpe & Falle 2011) was used. The mesh was refined by a factor of two in both directions whenever a relative tolerance of 1% was exceeded between existing mesh levels for density, pressure or velocity. The refinement was extended five to ten cells in all directions from the cell needing refinement. Figure 9 shows the resulting adaptive mesh in viscous and inviscid simulations. A maximal resolution of 16 points per mean free path in the unshocked gas was used. Under the conditions of experiment 9, for example, the mean free path of the test gas was $0.56 \mu\text{m}$ (before being shocked). At maximum resolution, the distance of one mean free path is covered by up to 16 grid points, resulting in a maximum resolution of 16 grid points per 0.56 , or $0.035 \mu\text{m}$ between every grid point. Figure 10 shows this resolution is sufficient to accurately reproduce shock wave thickness.

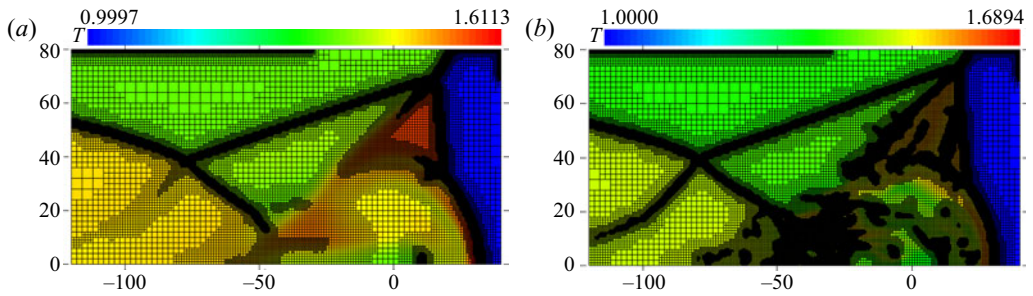


FIGURE 9. Adaptive computational mesh overlaid on a temperature plot ($M = 3.5$, $\gamma = 1.06$, $t = 132$). (a) Viscous and (b) inviscid.

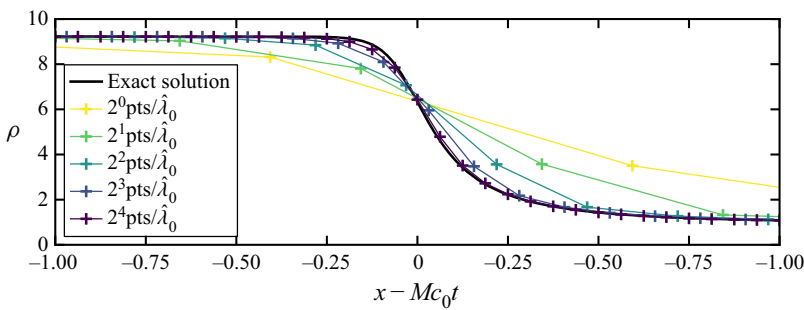


FIGURE 10. Comparison of shock profiles evolved from a discontinuity to $t = 4$ at different resolutions and the steady solution of the Navier–Stokes equations ($M = 3.5$, $\gamma = 1.06$).

The Navier–Stokes shock structure recovers the experimental and direct simulation Monte Carlo results at low Mach numbers but deteriorates at moderate and higher Mach numbers (Uribe & Velasco 2018). The lack of phenomenological models that can recreate the strong shock structure remains an open problem. The purpose of using shock-resolved Navier–Stokes simulations is to remove the solution’s dependence on solver type and to ensure the correct Navier–Stokes solution is reached for all larger features, such as the slip line, forward jet, vortex and their interaction with the shock front. It also provides properly resolved results for future shock reflection studies which may seek to compare other models or simulations with reduced resolutions. Simulating shock reflection using direct simulation Monte Carlo methods would be a further improvement, but these are even more computationally demanding. The Navier–Stokes simulations require much computational time due to the high resolution and the viscous Courant–Friedrichs–Lewy (CFL) criterion. As a result, the viscous simulations were limited to $\gamma = 1.06$. Reflections at this isentropic exponent have short Mach stems which permits the use of small domains, and their Reynolds numbers grow quickly thus necessitating fewer time steps. The maximum time step size was determined using the CFL condition with $CFL = 0.4$ on the refined meshes.

The initial conditions consisted of a triple-shock, calculated using the ideal three shock theory, whose triple point was imposed above a symmetry boundary, as illustrated in figure 11(a). The large arrows point from the post-shock state to the pre-shock state. The initial conditions can be recreated using the data from table 3 employing the shock Mach numbers with the Rankine–Hugoniot equations, the angles w between discontinuities and the reference frame speed u_0 (post-reflection Mach stem speed, calculated using three

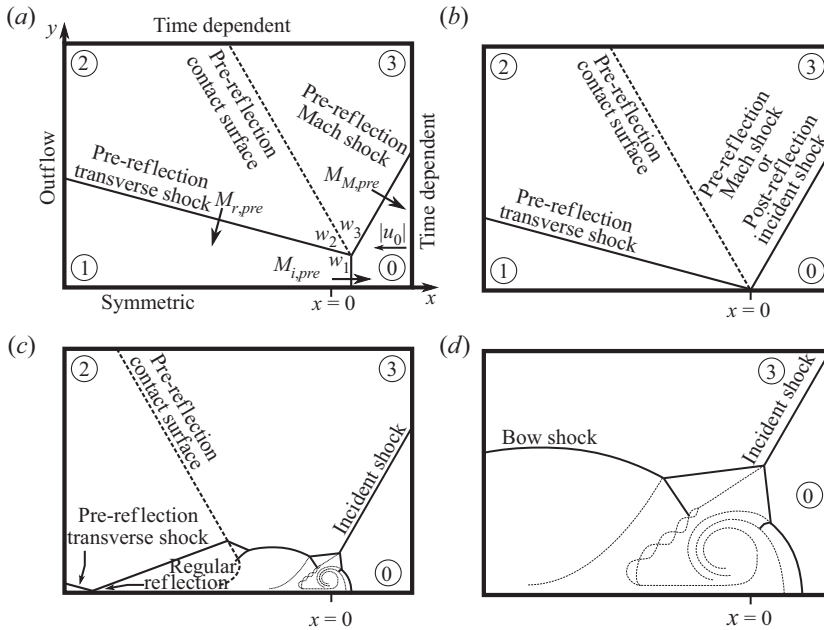


FIGURE 11. Initial and boundary conditions of simulations, and triple-shock reflection; ① unshocked state, ① pre-reflection incident shock state, ② pre-reflection transverse shock state, ③ pre-reflection Mach shock state and post-reflection incident shock state. (a) $t = -1$: initial and boundary conditions; (b) $t = 0$: triple point reaches reflecting surface; (c) $t > 0$: Mach reflection forms and grows; (d) $t \gg 0$: pre-reflection features leave domain.

$M_{M,pre}$	$M_{i,pre}$	$M_{r,pre}$	u_0	w_1	w_2	w_3
2.5	2.03663	1.22304	-3.14027	104.462°	44.6553°	60.8829°
3	2.45729	1.21608	-3.74700	118.124°	36.2915°	55.585°
3.5	2.45762	1.21592	-3.74647	118.108°	36.2434°	55.6491°
4	3.30702	1.20460	-4.95286	140.018°	24.1620°	45.8199°
5	4.16138	1.19658	-6.15981	141.205°	23.5999°	45.1955°
6	5.01458	1.19159	-7.36482	145.904°	21.2707°	42.8248°

TABLE 3. Initial conditions for triple-shock simulations (see figure 11); pre-reflection shock Mach numbers are listed so $M_i = M_{M,pre}$; $\gamma = 1.06$, $v_0 = 0$, $p_0 = 1$, $\rho_0 = 1$, $w_0 = 150^\circ$.

shock theory). Using a triple shock as initial condition does away with non-physical leaky boundary conditions and provides an unambiguous way to pose the problem (Lau-Chapdelaine & Radulescu 2016). It also closely resembles triple-shock reflections in detonations.

In this configuration, the triple point initially moves downwards and to the left (figures 11a to 11b) because the pre-reflection incident shock is slower than u_0 . The initial distance of the triple point above the symmetry boundary was chosen to allow the viscous shock structures to develop before reflection. The triple point reaches the origin on the symmetry boundary at $t = 0$ (figure 11b) and reflects. The pre-reflection Mach stem (the oblique shock between states ① and ③, figure 11b) becomes the post-reflection incident

shock and a Mach reflection is formed (figure 11c). The pre-reflection slip line, incident and transverse shocks are washed out to the left because they travel slower than the frame of reference (figures 11c to 11d).

The top and right boundaries were functions of time, moving the initial shock and slip line states along the boundaries. An outflow condition with zero normal gradient was used on the left boundary. The domain was sized to fit the double Mach reflection structure at the target simulation time. The remaining parts of the reflection (e.g. bow shock; figure 11d) were allowed to flow out of the domain. Comparison of different domain sizes showed the domains chosen were sufficiently large to have no effect on the phenomena being studied.

The target simulation time was found for a desired Reynolds number of $Re_{target} = 1000$, defined in (2.1). The Mach stem height was estimated *a priori* from three shock theory as $h = \tan(\chi)M_M c_0 t$, with post-reflection triple-point path angle χ , post-reflection Mach stem Mach number M_M and unshocked sound speed c_0 . This yields an expression for the target time:

$$t_{target} = \frac{v_{mean}}{u_{shear} \tan(\chi) M_M c_0} Re_{target}, \quad (3.3)$$

where v_{mean} and u_{shear} are also estimated from three shock theory. The solution was exported at fixed time steps throughout the simulation. Reaching the target time for $M_i = 2.5$ in a domain measuring $352 \times 192 \lambda_0$ took approximately 20 days on 60 AMD Opteron 6282 processor cores with a coarse grid of 22×12 cells and 8 levels of refinement, for a finest possible grid of 5632×3072 cells. The computational resources limited the scope of simulations to $Re \sim 10^3$, smaller than those of the experiments by a factor of 10 to 10^3 , because the computational effort scales with the cube of the target Reynolds number. The gap between shock-resolved viscous simulations and experiments remains to be bridged.

Inviscid simulations of triple-shock reflection were performed under the same conditions, but without viscosity or heat conduction. The same resolution, number of refinement levels and refinement criteria were used, and they were marched to the same time as their viscous counterparts.

3.2. Viscous simulation results

Plots of temperature are presented in figure 12. Each row represents one simulation at the Mach number specified in the first column. The Reynolds number is increased from ≈ 30 to ≈ 110 and ≈ 1000 in each column. The Reynolds number is measured the same way as in experiments: (2.1) is used with the shear velocity and viscosity from three shock theory and the Mach stem height is measured from the results. The temperature scales on the right range from the incident shock temperature to the maximal temperature in the simulation. They apply to each panel in the row. The panels are cropped to the region of interest around the jet, vortex and Mach stem.

The triple-shock reflection with an incident shock of $M_i = 2.5$ is shown in figure 12(a–c). The Mach stem at $Re = 34$ is smoothly curved from the triple point to the reflecting surface and straightens as Reynolds number increases. The forward jet grows with Reynolds number and develops a vortex by $Re \approx 1000$; however, the head of the forward jet remains far from the Mach stem.

The jet is closer to the Mach stem at $M_i = 3.0$. The jet reaches the Mach stem and causes it to bulge when $Re \approx 1000$, and eventually bifurcate when $Re > 1200$. The vortex at the head of the jet is larger than the previous case.

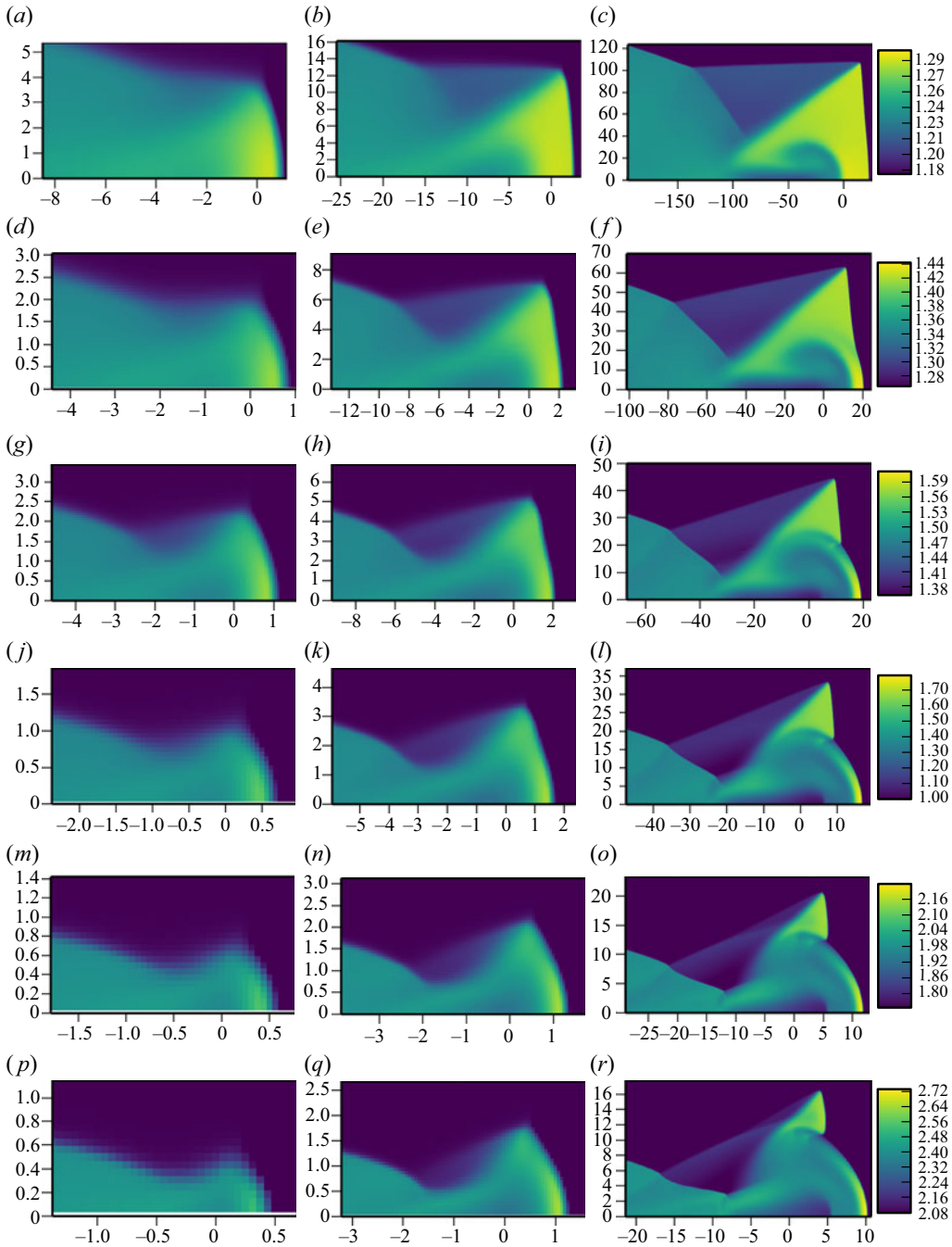


FIGURE 12. Temperature plots of viscous simulations ($\gamma = 1.06$, $\theta_w = 30^\circ$): (a) $M_i = 2.5$, $Re = 34$, $t = 12$; (b) $Re = 114$, $t = 36$; (c) $Re = 1014$, $t = 276$; (d) $M_i = 3.0$, $Re = 29$, $t = 6$; (e) $Re = 108$, $t = 18$; (f) $Re = 993$, $t = 138$; (g) $M_i = 3.5$, $Re = 48$, $t = 6$; (h) $Re = 118$, $t = 12$; (i) $Re = 1022$, $t = 87$; (j) $M_i = 4.0$, $Re = 32$, $t = 3$; (k) $Re = 103$, $t = 7.5$; (l) $Re = 1029$, $t = 60$; (m) $M_i = 5.0$, $Re = 31$, $t = 2$; (n) $Re = 101$, $t = 4.5$; (o) $Re = 965$, $t = 33$; (p) $M_i = 6.0$, $Re = 29$, $t = 1.5$; (q) $Re = 106$, $t = 3.5$; (r) $Re = 1010$, $t = 24$.

At $M_i = 3.5$, the forward jet is strong enough to cause a change of curvature in the Mach stem by $Re \approx 110$, and the Mach stem bifurcates when $Re > 440$, as seen in [figure 12\(i\)](#). Only a portion of the Mach stem is straight below the triple point. A new triple point is located about midway on the Mach stem, below which the Mach stem is curved. The vortex is large enough that it causes the slip line to deflect downwards. Double Mach reflections with a Mach stem bifurcation have been classified as triple Mach–White reflections by Semenov, Berezkina & Krasovskaya (2009a).

The trend continues as Mach number is increased: the jet moves closer to the Mach stem, causing the Mach stem to deform and bifurcate as early as $Re \approx 200$. The jet terminates in an increasingly large vortex that dominates the space behind the Mach stem. The vortex grows large enough to interfere with the slip line and flow behind the reflected shock.

3.3. Inviscid simulation results

The Euler equations are typically used to simulate shock reflections and detonations. These ‘inviscid’ simulations suffer from numerical dissipation that depends on grid and scheme, not a physical phenomenon. However, inviscid simulations are much faster to compute and offer insight into how the reflection will evolve as Reynolds number becomes very large.

Temperature plots of inviscid simulations are shown in [figure 13](#). The first row shows results for $M_i = 2.5$. The inviscid double Mach reflection at $t = 12$ resembles the viscous case in [figure 12\(c\)](#), but with Kelvin–Helmholtz instabilities along the slip line and a vortex that has completed more than one rotation. As time increases, the forward jet and vortex move closer to the Mach stem, causing a change of curvature on the Mach stem but no bifurcation. Kelvin–Helmholtz instabilities grow along the slip line, forward jet and vortex.

The following rows of [figure 13](#) show the effect of increasing Mach number. The jet approaches, deforms and bifurcates the Mach stem; the vortex becomes large enough to disrupt the slip line, and a shock develops in the forward jet. Kelvin–Helmholtz instabilities become more prevalent in the vortex, resulting in a heterogeneous temperature field behind the Mach stem.

At larger Mach numbers ($M_i \geq 4.5$) the bifurcation point is disproportionately elevated at early times (e.g. [figures 13j](#) to [13l](#)). Here the bifurcation point moves up-and-down and the Mach stem foot rocks to-and-fro, leading to instances where the Mach stem bulge appears flattened, like in [figure 13\(l\)](#). However, the shape of the bifurcated Mach stem generally remains similar to that in [figure 12\(r\)](#), composed of a straight Mach shock and round bulge.

3.4. Summary of simulations

The reflection of a triple point from an axis of symmetry was simulated for $M_i = 2.5$ to 6, $\gamma = 1.06$, $\theta_w = 30^\circ$ and $Re \leq 2 \times 10^3$. Reynolds number was found to play an important role in the development of the shock reflection. Forward jetting and the vortex size increased with Reynolds number and Mach number. Interaction of the jet with the Mach stem led to bulging and bifurcation of the Mach stem. Inviscid simulations developed Kelvin–Helmholtz instabilities and heterogeneous temperature fields in the vortex behind the Mach stem that were absent from the viscous results. Varying the Mach number led to the same changes that were seen in experiments.

4. Discussion

The experiments and numerical simulations are compared in the next two subsections. A qualitative comparison of the shock structures is made in §4.1, followed by a

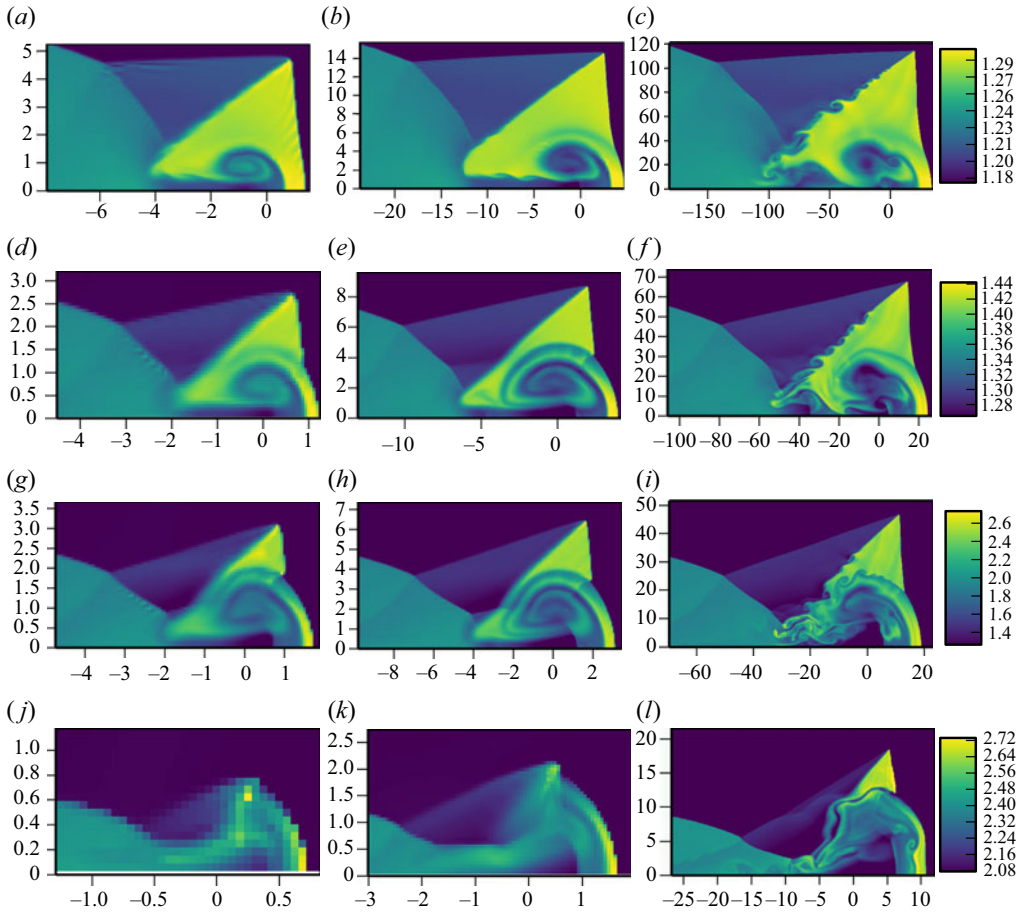


FIGURE 13. Temperature plots of inviscid simulations ($\gamma = 1.06$, $\theta_w = 30^\circ$): (a) $M_i = 2.5$, $t = 12$; (b) $t = 36$; (c) $t = 276$; (d) $M_i = 3.0$, $t = 6$; (e) $t = 18$; (f) $t = 138$; (g) $M_i = 3.5$, $t = 6$; (h) $t = 12$; (i) $t = 84$; (j) $M_i = 6$, $t = 1.5$; (k) $t = 3.5$; (l) $t = 24$.

comparison of bulging and jetting, and of numerical triple-point paths. Mach stem bifurcation is compared in § 4.2 then explored in further depth using inviscid simulations.

The reader should remain cognizant of differences between viscous simulations where $Re \lesssim 10^3$, inviscid simulations that hint at larger Reynolds numbers and unsteady experiments where $Re \sim 10^5$. The viscous simulations resemble triple-shock reflections that occur at the beginning of a detonation cell, and the experiments, which include shock curvature, are a better representation of the reflection process later in the detonation cell cycle. Differences between individual simulations and experiments are to be expected. However, the effects that lead to a strong forward jet, vortex and jet–shock interaction can be inferred by comparing the three sets of results while considering their similarities, their trends and the unique ways they differ.

4.1. Comparison of results

Experiments and simulations are qualitatively compared in figure 14. As predicted by three shock theory and observed in all cases, increasing Mach number shortens the Mach stem

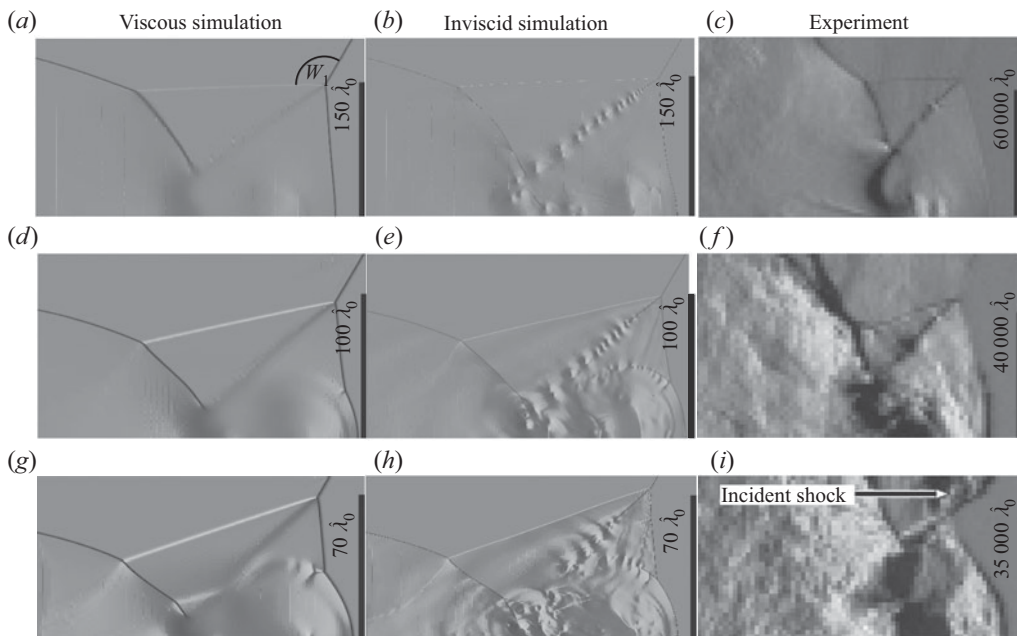


FIGURE 14. Comparison of viscous (*a,d,g*) and inviscid (*b,e,h*) simulations with experiments (*c,f,i*) ($\gamma = 1.06$, $\theta_w = 30^\circ$); scale shown by vertical black bar : (*a*) $M_i = 2.5$, $Re = 1340$; (*b*) $M_i = 2.5$; (*c*) $M_c = 2.5$, $Re = 6.8 \times 10^5$; (*d*) $M_i = 3.0$, $Re = 1481$; (*e*) $M_i = 3.0$; (*f*) $M_c = 2.7$, $Re = 5.2 \times 10^5$; (*g*) $M_i = 3.5$, $Re = 1600$; (*h*) $M_i = 3.5$; (*i*) $M_c = 3.4$, $Re = 7.5 \times 10^5$.

and increases the reflected shock angle w_1 . More pertinent to this study, increasing the Mach number also increases the forward jet, vortex and bulging size in all cases. The forward jet catches up to the shock front ($M \geq 2.7$), causing it to deform in the experiment ($M_c = 3.4$) and clearly bifurcate in simulations.

The forward jet length, size of the vortex and the shock reflection structure are qualitatively alike in the inviscid simulations and the viscous simulations at $Re > 1000$. However, the inviscid simulations contain Kelvin–Helmholtz instabilities that significantly change the flow field in the jet and vortex behind the Mach stem. The instabilities cause rough-looking features in the flow field behind Mach stem in experiments and inviscid simulations, but are absent from viscous simulations. This means Reynolds number plays an important role in the development of large-scale mixing behind the Mach stem.

The extent of forward jetting and Mach stem bulging in simulations are quantified in [figure 15](#) as functions of the Reynolds and Mach numbers. They are measured as the horizontal distance between the triple point and the jet's head, or Mach stem position along the reflecting surface, respectively, and normalized by the Mach stem height. The amount of viscous bulging on the left of [figure 15\(a\)](#) is compared to the average inviscid value on the right, sharing the ordinate axis. [Figure 15](#) shows that the viscous Mach stem and jet overtake the triple point as Mach number and Reynolds number are increased. The jet size and amount of bulging grow in tandem once the jet passes the triple point. The amount of bulging converges towards the mean inviscid value.

The Mach stem bulges more in simulations than experiments ([figure 8c](#)). While some difference is to be expected due to the experiments' unsteadiness and large Reynolds numbers, the difference remains to be reconciled. It is worth noting that three-dimensional

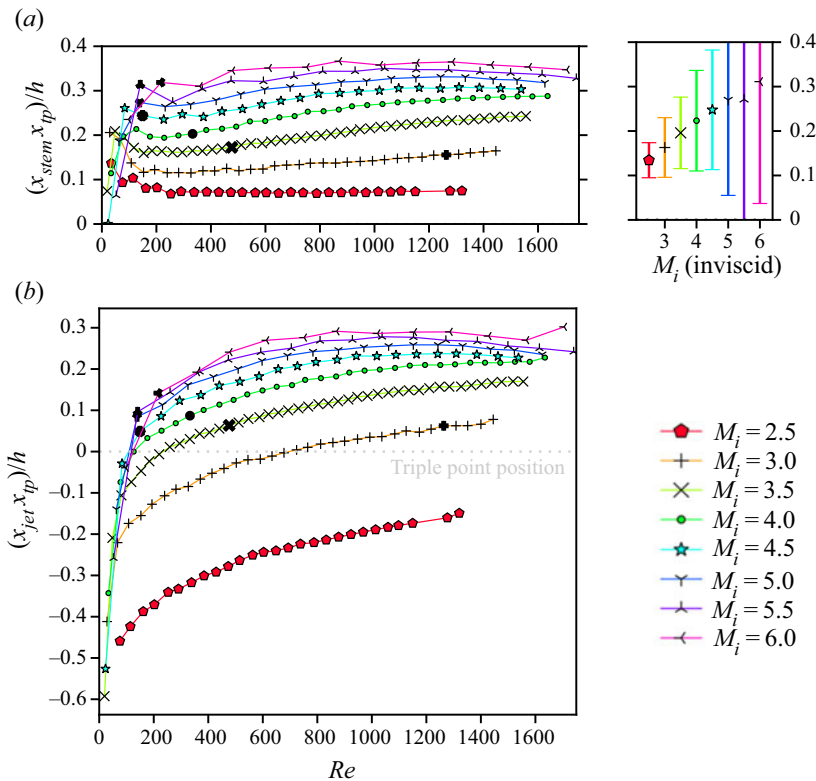


FIGURE 15. Evolution of the Mach stem and jet at the reflecting surface from simulations ($\gamma = 1.06$, $\theta_w = 30^\circ$); bold points where bifurcation is first observed; error bars at 3 standard deviations. (a) Mach stem position; left: viscous; right: inviscid. (b) Viscous jet position.

effects caused by the shallow channel depth (19.1 mm) are not responsible for this difference. In experiment 9, for example, while the shock travels 200 mm from the tip of the obstacle, boundary layers on the channel windows grow only 0.7 mm (Fay 1959) from the shock to the rear of the jet. The boundary layers do not intersect across the jet.

Another clear and easily quantifiable measure is the median instantaneous angle χ between the triple-point path and the horizontal plotted in figure 16. Experimental results are omitted due to their unsteadiness. The difference between viscous and inviscid simulations is less than 1° , suggesting viscosity has little effect on the triple-point path. Three shock theory underestimates χ in the simulations by 1° to 3° , increasing with Mach number, which is on a par with its underestimation of experiments (Ando 1981; $\gamma = 1.29$). This may be explained by the idealistic assumption that the Mach stem is perpendicular to the reflecting surface (Li & Ben-Dor 1999).

4.2. Mach stem bifurcation limits

Triple Mach–White reflections (Semenov *et al.* 2009a) are characterized by the appearance of a new triple point that bifurcates the Mach stem; however, there is little data (Mach 2011) on its limits. The limits of Mach stem bifurcations are explored in this section as a function of M , θ_w , γ and Re .

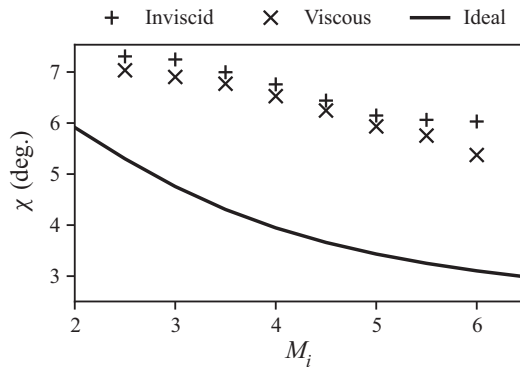


FIGURE 16. Angle of the triple-point path with respect to the reflecting surface from three shock theory, viscous and inviscid simulations ($\gamma = 1.06, \theta_w = 30^\circ$).

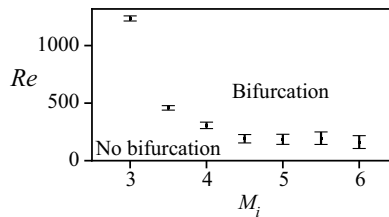


FIGURE 17. Onset of Mach stem bifurcation in viscous simulations ($\gamma = 1.06, \theta_w = 30^\circ$).

The Reynolds number where Mach stem bifurcation is first observed is displayed in figure 17. Bifurcation occurs at Reynolds numbers above the points in the plot, while the Mach stem remains unbifurcated below. The plot points to a minimum Mach number, $M_i < 3$, below which bifurcation does not occur when $\gamma = 1.06$ and $\theta_w = 30^\circ$. These novel results show that Mach stem bifurcation is sensitive to Reynolds number near the minimum Mach number, whereas bifurcations at high Mach numbers occur early in the reflection, once $Re \gtrsim 200$. These points are plotted in bold in figure 15, revealing that bifurcations occur when the jet overtakes the triple point by $(x_{jet} - x_{tp})/h \gtrsim 5\%$ (for $\gamma = 1.06, \theta_w = 30^\circ$). The presence of Mach stem bifurcation serves as an indication of the jet’s strength.

There is agreement between inviscid simulations and viscous simulations at $Re \gtrsim 1000$ regarding the shape of the shock reflection, the triple-point path angle and the amount of Mach stem bulging. Additionally, Mach stem bifurcation occurs between $2.5 \leq M_i < 3$ in both cases. This motivates the use of inviscid simulations to estimate the bifurcation limits, and the amount of jetting by proxy, over a range of reflection angles and isentropic exponents that would be computationally expensive to calculate with viscosity.

A resolution study is first performed, since the lack of scale in the Euler equations makes it ambiguous to know for how much time the inviscid simulations should be run. Figure 18 shows inviscid simulations near the bifurcation limit at target times calculated using (3.3), with $Re_{target} = 100$ (figure 18a–c) and an $Re_{target} = 1000$ (figure 18d–f). The latter case has about ten times more grid points resolving the Mach stem height. The schlieren plots are inspected for the presence of a transverse shock wave on the Mach stem, as indicated in figure 18, and the Mach stem is considered to have bifurcated if one is found. This is similar to how transitional and double Mach reflections were differentiated in past work.

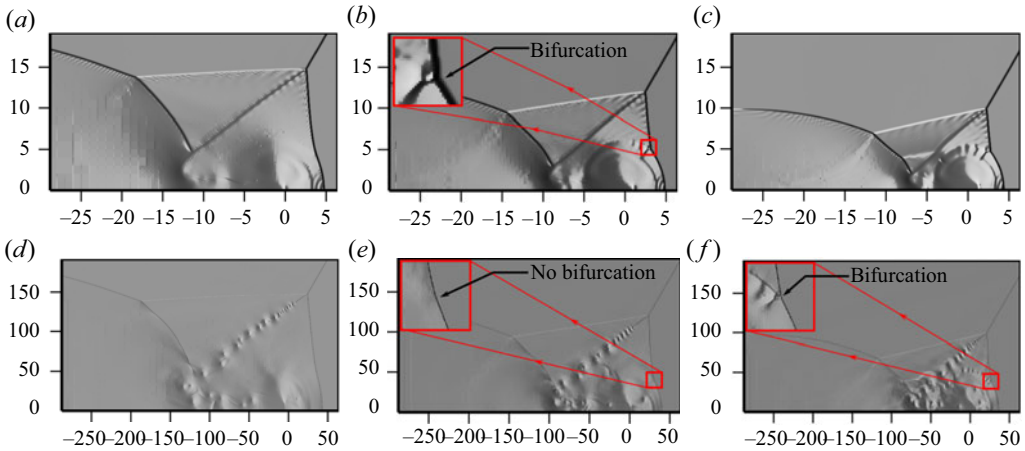


FIGURE 18. Comparison of inviscid simulations across the bifurcation boundary at times equal to viscous triple-shock calculations with $Re_{target} = 100$ (a–c) and 1000 (d–f), $\gamma = 1.06$, $\theta_w = 30^\circ$; insets are magnifications of the Mach stem. (a) $M_i = 2.5$, $t = 36.3$; (b) $M_i = 2.75$, $t = 26.5$; (c) $M_i = 3$, $t = 20.3$; (d) $M_i = 2.5$, $t = 363$; (e) $M_i = 2.75$, $t = 265$; (f) $M_i = 3$, $t = 203$.

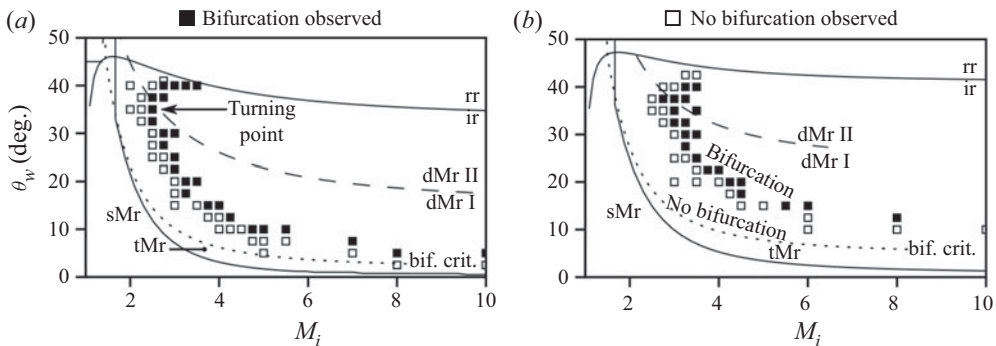


FIGURE 19. Mach stem bifurcation domain from inviscid simulations; rr: regular reflection; ir: irregular reflection; sMr: single Mach reflection; tMr: transitional Mach reflection; dMr: double Mach reflection, cases I and II; bif. crit.: analytic bifurcation criterion (Mach 2011; bifurcations predicted above, no bifurcations below). (a) $\gamma = 1.06$ and (b) $\gamma = 1.15$.

No bifurcation is found at $M_i = 2.5$, and a bifurcation is found at $M_i = 3$ at both resolutions. The $M_i = 2.75$ case is critical, with the bifurcation at $t = 26.5$ disappearing by $t = 265$. This critical behaviour is to be expected near the bifurcation limit since the phenomenon is sensitive to diffusion and affected by the appearance of Kelvin–Helmholtz instability. Using $Re_{target} = 100$ to calculate simulation time is sufficient to recover the bifurcation limit found in viscous reflections at $Re \approx 1000$, within ± 0.25 of the Mach number in this case.

The computations are extended to a larger range of M , θ_w and γ and plotted in figures 19 and 20. Each square represents one simulation; filled squares show simulations with a bifurcated Mach stem and open squares indicate simulations without one. The Mach stem bifurcation limit lies on the boundary between filled and open squares.

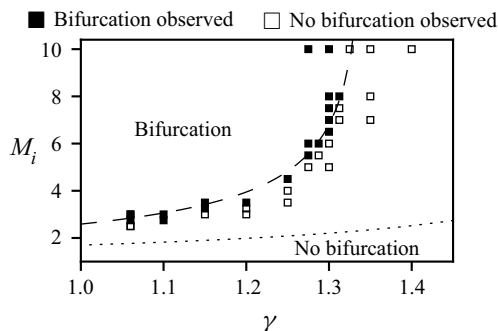


FIGURE 20. Mach stem bifurcation domain from inviscid simulations at a fixed angle ($\theta_w = 30^\circ$); dotted: analytic bifurcation criterion (Mach 2011); dashed: shock Mach number for a density ratio of 6.7.

Figure 19 shows the effect of Mach number and reflection angle on Mach stem bifurcations. The inviscid results match the bifurcation limit of viscous simulations ($2.5 < M_i \leq 3$, $\gamma = 1.06$, $\theta_w = 30^\circ$) and are in agreement with the onset of Mach stem deformation found in the experiments ($2.9 < M_c \leq 3.5$ for $\gamma_0 = 1.15$ and $2.7 < M_c \leq 3.4$ for $\gamma_0 = 1.06$, $\theta_w = 30^\circ$). The $\gamma = 1.15$ limit also lies close to the experimental limit of $3.84 < M_i \leq 4.09$ at $\gamma_0 = 1.13$ and $\theta_w = 15^\circ$ found by Semenov *et al.* (2009b).

A number of curves are plotted along with the simulation results in figure 19 to help locate where Mach stem bifurcations begin relative to other types of shock reflection. The curves delimit other shock reflection boundaries: the sonic criterion of the regular reflection boundary (ir/rr) is plotted at the top with a solid nearly horizontal curve. Mach reflections do not occur above this curve. The lower solid curve connected to the vertical line represents the single/transitional Mach reflection boundary (sMr/tMr). Transitional and double Mach reflections occur above this curve. Details of these limits are available in Ben-Dor (2007).

The dashed curve identifies the boundary between cases I and II of the double Mach reflection (dMr I/II), defined by Li & Ben-Dor (1995). Case I lies below the curve and case II is above. The flow around the secondary triple point in a double Mach reflection can be calculated using three shock theory, with an assumption about the angles between the shocks. In a type I double Mach reflection, the secondary reflected shock is assumed to be straight and to intersect the slip line at a right angle (e.g. figure 12c). A type II double Mach reflection occurs when this assumption would put the intersection point below the reflecting surface, so the secondary reflected shock is assumed to form a straight line between the secondary triple point and the intersection of the slip line with the reflecting surface.

The dMr I/II boundary fits well with a turning point of the bifurcation limit. Mach (2011) postulated that the secondary reflected shock of a type II double Mach reflection would prevent bifurcation, by turning the jet away from the Mach stem; however, the transition from I to II only shifts the bifurcation limit to higher Mach numbers.

The dotted line in figure 19 (bif. crit.) is an analytic bifurcation criterion proposed by Mach (2011). It is based on the idea that the slip line must eventually become parallel to the wall (Hornung 1986). When pressure from the flow deflection process (flow passing the over wedge tip) exceeds pressure from the shock reflection process, a stagnation point is created near the slip line, driving streamlines to its right into the forward jet. The speed of flow in the jet is compared to the Mach stem speed and if the jet is faster than the

Mach stem, bifurcation is assumed to occur. Li & Ben-Dor (1999) and Shi *et al.* (2019) performed similar analyses to account for bulging (not bifurcation) of the Mach shock. This criterion underestimates the Mach number and wedge angle required for bifurcation and performs poorly at higher isentropic exponents.

The dependence of the bifurcation boundary on the isentropic exponent is explored in M_i - γ phase space in figure 20 for $\theta_w = 30^\circ$. The Mach number required for bifurcation increases with isentropic exponent until $\gamma \approx 1.3$ is reached. Strong jets that bulge the Mach stem are still present above this value, but no bifurcations are observed despite Mach's bifurcation criterion (dotted curve, Mach (2011)) predicting otherwise. This lack of limit in Mach's bifurcation criterion suggests that there is a missing link between jetting and bifurcation. A better criterion is required for predicting the triple Mach–White reflections.

4.3. Implication to detonation structure

Shock reflections have been shown to contribute to the propagation of detonations (Lee 2008). Detonations are supersonic combustion waves that suffer from a multidimensional instability that causes their shock front to be punctuated by triple points. The triple points periodically reflect from each other, creating new triple points. A curved Mach stem is formed upon reflection, like in the experiments, and the new triple points go on to collide with their neighbours. The Mach stem becomes the incident shock for the next reflection and the process repeats. The experiments' curved shocks form a nice analogue to the unsteady shock reflection process in detonations.

Tracing the triple-point paths of a detonation creates a pattern of interlocking diamonds called the cellular detonation structure. Detonations are often characterized by the size and regularity of their cellular structure. Detonations with irregular structures are more resistant to quenching and their mixtures are easier to detonate than regular ones (Moen *et al.* 1986; Radulescu & Lee 2002).

Radulescu *et al.* (2009), Mach (2011) and Mach & Radulescu (2011) suggested that Mach stem bifurcation may contribute to the irregularity of the detonation cellular structure by creating new detonation cells. They showed that bifurcations contribute to an irregular appearance on numerical soot foils of detonations. They tabulated 21 experiments from other work and categorized the cellular structure as regular, intermediate and irregular and found perfect agreement between regular detonations and the absence of bifurcation in their inviscid simulations. A clear distinction can be made from their tabulated data: irregular and intermediate structures arise when $\gamma_1 \leq 1.32$ and regular structures occur when $1.41 \leq \gamma_1$. This closely matches the bifurcation limit of $\gamma \approx 1.3$ found in this study.

The detonability and quenching resistance exhibited by irregular mixtures may be a result of the strong jetting and large-scale mixing that occurs behind the Mach stem in gases with low isentropic exponents. Experiments show that this mixing becomes especially evident when Kelvin–Helmholtz instabilities are entrained into the vortex. In detonations, reaction rates behind the Mach stem will be sensitive to the presence of mixing and turbulence, predominantly near detonation propagation limits. A parametric investigation of the effect of isentropic exponent on mixing in detonations and their cellular structure would be of particular interest.

4.4. Shock instability at high Mach number and low isentropic exponent

The textured appearance of the schlierens behind the incident, reflected and Mach shocks seen in certain experiments (e.g. figures 4g, 5d and 5g) indicates a non-uniform

density field. The flow field becomes less uniform as the isentropic exponent is decreased from $\gamma_0 = 1.15$ to 1.06 and as the Mach number is increased. The non-uniformity is not caused by contamination of the test section by driver gas. This is evidenced by the fact the bow shocks remain intact and attached to the chevron, as discussed in § 2.2.4. Furthermore, simulations in the [appendix](#) show that the driver–test gas interface is far from the leading shock in all experiments when the full stand-off distance of $\hat{\lambda}_d = 1.85$ is used. The cause of the phenomenon is not understood but may be linked to shock wave instability.

Shock wave instability has been ascribed to endothermic processes such as ionization (Griffiths, Sandeman & Hornung 1976; Glass & Liu 1978; Grun *et al.* 1991) and dissociation (Griffiths *et al.* 1976), or to heavy gases (i.e. low-isentropic-exponent gases) where vibrational relaxation may occur behind the shock (Griffiths *et al.* 1976; Mishin *et al.* 1981; Hornung & Lemieux 2001; Semenov *et al.* 2009*b*; Ohnishi *et al.* 2015). Shock instability has been observed by Sirmas & Radulescu (2015, 2019) in molecular dynamic calculations of relaxing shock waves in gases with inelastic collisions, as would occur where strong vibrational relaxation effects are present. Work with hypersonic projectiles has attributed similar shock instability to vibrating or unstable contact surfaces. Experiments and simulations of Hornung & Lemieux (2001) and Ohnishi *et al.* (2015) found instability when density jumps of $\rho_1/\rho_0 \geq 14$ and $\rho_1/\rho_0 \geq 10$ were reached across the shock. Interestingly, the bifurcation boundary in M – γ space is well represented by a constant density ratio of $\rho_1/\rho_0 = 6.7$ across the shock, plotted with a dashed curve in [figure 20](#).

The stability of these low-isentropic-exponent gases is of interest and should be investigated in future work. This could be done by introducing vibrational relaxation effects into simulations, for instance, as the instability was not seen in the Navier–Stokes simulations.

5. Conclusion

Experiments and simulations were used to study the effect of the isentropic exponent, Mach number and Reynolds number on the large-scale convective mixing caused by the forward jet, vortex and flow behind the Mach stem. Experiments were performed over a limited range of Mach numbers at large Reynolds numbers ($Re \sim 10^5$) and various isentropic exponents. Viscous simulations were performed for a larger range of Mach numbers but were limited to small Reynolds numbers ($Re \sim 10^3$) and $\gamma = 1.06$. Inviscid simulations were used to bridge the gap between viscous simulations and experiments; however, differences between simulations and experiments remain to be reconciled.

In all cases, as the isentropic exponent decreased, or the Mach number or Reynolds number increased, the forward jet approached the Mach stem and developed a vortex. The jet and vortex can grow strong enough to completely disrupt the flow field behind the Mach shock, and cause the Mach stem to bulge once jet–shock interaction becomes important.

The region behind the Mach stem continuously evolves as Reynolds number is increased. A turbulent structure becomes visible behind the Mach stem in experiments when the isentropic exponent is sufficiently small and the Mach number is sufficiently large. Similar heterogeneous flow fields are observed in inviscid simulations. This is attributed to Kelvin–Helmholtz instability in the vortex, and is absent from the viscous results. The experiments clearly show that large-scale convective mixing behind the Mach stem is driven primarily by low isentropic exponents. When the isentropic exponent is too large, e.g. $\gamma = 1.4$, neither jet–shock interaction nor large-scale mixing are observed.

The limits of Mach stem bifurcation (triple Mach–White reflection) have been reported in θ_w – M_t – γ phase space. Bifurcations are found to be absent when $\gamma \gtrsim 1.3$ at $\theta_w = 30^\circ$, a limit which corresponds closely to the boundary between regular and irregular cellular structures of detonations. The detonability and quenching resistance of irregular mixtures may be a result of the strong jetting and large-scale mixing that occurs behind the Mach stem in gases with low isentropic exponents.

Acknowledgements

The authors thank S. Falle from the University of Leeds for generously allowing the use of his computational code *mg* which made the numerical simulations possible. The authors acknowledge financial support from the Natural Sciences and Engineering Research Council of Canada (NSERC) through the Discovery Grant ‘Predictability of detonation wave dynamics in gases: experiment and model development’ (2017–2022).

Declaration of interests

The authors report no conflict of interest.

Supplementary movies

Supplementary movies are available at <https://doi.org/10.1017/jfm.2020.731>.

Appendix. Simulations with varying diaphragm stand-off distances

Inviscid simulations of the shock tube and obstacle were performed to assess the diaphragm stand-off distance and to gauge the effect of the driver–test gas interface on the shock reflection.

The two-dimensional domain spanned half the shock tube height, from the centre line to the shock tube wall, five half-heights upstream of the chevron tip and three half-heights downstream. The domain was covered by a 40×5 coarse grid with six levels of refinement for a finest possible grid of 2560×320 and resolution of 3.15 grid points per millimetre. The chevron was created with a step-like boundary. Step boundaries have been shown to affect the shock reflection configuration (Ben-Dor *et al.* 1987), but perform decently (Falle & Giddings 1992) with sufficient dissipation (controlled here by low resolution). The top and bottom boundaries employed symmetry conditions, and the left and right boundary had zero normal gradients. The origin was located at the trailing edge of the chevron. The simulations were initiated with a shock located at $\hat{x}_{s,0} = -15.24$ cm. The driver gas was initially at $\hat{x}_{d,0} = u_t/D_t(\hat{x}_{s,0} - \hat{l}_d) + \hat{x}_{s,0}$, where $D_t = M_t c_0$ is the shock speed and u_t is the shocked particle speed. The driver gas has the same pressure and velocity as the shocked gas, but with a density of $2\rho_0$.

Experiment 9 (see table 1, $M_c = 3.4$ and $\gamma = 1.06$) is simulated because it is the most compressible (i.e. highest Mach number and lowest isentropic exponent) of all experiments with a stand-off of $\hat{l}_d = 1.85$ m. If this experiment is unaffected by the driver–test gas interface, then so are all the other experiments where $1.06 \leq \gamma_0$, $M_c \leq 3.4$ and $\hat{l}_d = 1.85$ m. An initial shock strength of $M_t = 4.2$ is required to generate a shock of $M_c = 3.4$ on the chevron.

The simulation results are presented in figure 21. The panels show schlieren images in the top halves. The bottom halves show temperature cutoff at $T = 1.6$ to emphasize details in the reflection. The x and y coordinates are scaled in metres.

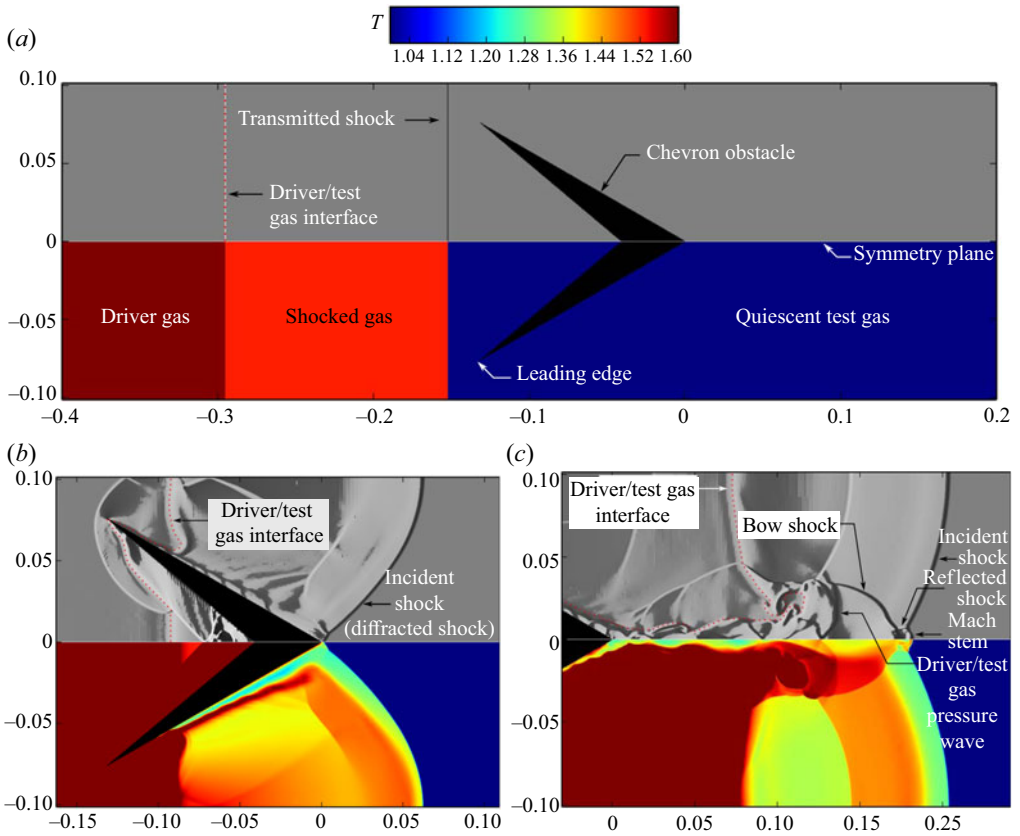


FIGURE 21. Inviscid simulation of shock reflection over a chevron ($\gamma = 1.06$, $M_c = 3.4$, $\hat{l}_d = 1.85$ m); top: schlieren; dotted red line: driver–test gas interface; bottom: temperature; axes scaled in metres. (a) Initial condition, before shock interaction with chevron; (b) shock diffracting over chevron; (c) shock reflection from plane of symmetry.

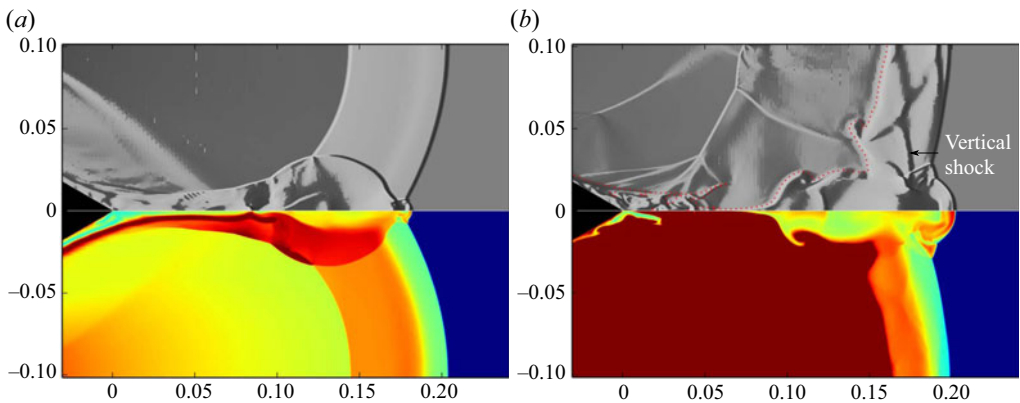


FIGURE 22. Inviscid simulations of shock reflection over a chevron ($\gamma = 1.06$); top: schlieren; dotted red line: driver–test gas interface; bottom: temperature; axes scaled in metres. (a) $M_c = 3.4$, no driver–test gas interface; (b) $M_c = 4.0$, $\hat{l}_d = 0.68$ m.

Figure 21(a) shows the initial conditions, i.e. after a shock has been transmitted through the diaphragm, but before it interacts with the obstacle. The driver–test gas interface is overlaid with a dotted red line. The shock diffracts over the chevron and reaches the trailing edge in figure 21(b). The driver–test gas interface remains far behind the shock front. The shock wave reflects from the axis of symmetry, forming a double Mach reflection with Mach stem bifurcation, as shown in figure 21(c). The driver gas has diffracted over the obstacle, driving a pressure wave that has not reached the front. When there is no driver–test gas interface (figure 22a), the shock front is identical to that of figure 21(c), showing that the driver–test gas interface does not interfere with the reflection front when $\hat{l}_d = 1.85$ m.

Figure 22(b) is a simulation of experiment 11 ($M_c = 4.0$ and $\gamma = 1.06$) where the stand-off distance was shortened to $\hat{l}_d = 0.68$ m. The driver–test gas interface is closer to the shock front and the double Mach reflection has a Mach stem that is clearly bifurcated and taller than the previous case, despite the higher Mach number. The bow shock (secondary Mach shock) travels much faster through the hot driver gas, forming a vertical shock.

These simulations demonstrate that the driver–test gas interface has no effect on the experiments with $\hat{l}_d = 1.85$ m, and that only experiments 10 and 11, where $\hat{l}_d < 1.85$ m, suffer from interference by the driver gas.

REFERENCES

- ANDO, S. 1981 Pseudo-stationary oblique shock-wave reflection in carbon dioxide-domains and boundaries. *Tech. Note* 231. University of Toronto Institute for Aerospace Studies.
- AUSTIN, J. M. 2003 The role of instability in gaseous detonation. PhD thesis, California Institute of Technology.
- BARBOSA, F. J. & SKEWS, B. W. 2002 Experimental confirmation of the von Neumann theory of shock wave reflection transition. *J. Fluid Mech.* **472**, 263–282.
- BEN-DOR, G. 2007 *Shock Wave Reflection Phenomena*. Springer.
- BEN-DOR, G., MAZOR, G., TAKAYAMA, K. & IGRA, O. 1987 Influence of surface roughness on the transition from regular to Mach reflection in pseudo-steady flows. *J. Fluid Mech.* **176**, 333–356.
- BHATTACHARJEE, R. R. 2013 Experimental Investigation of detonation re-initiation mechanisms following a mach reflection of a quenched detonation. Masters thesis, University of Ottawa.
- FAGHRI, A. & ZHANG, Y. 2006 *Transport Phenomena in Multiphase Systems*. Elsevier.
- FALLE, S. A. E. G. 1991 Self-similar jets. *Mon. Not. R. Astron. Soc.* **250** (3), 581–596.
- FALLE, S. A. E. G. & GIDDINGS, J. R. 1992 Body capturing using adaptive Cartesian grids. In *Numerical Methods for Fluid Dynamics* (ed. K. W. Morton), pp. 335–342. Clarendon Press.
- FALLE, S. A. E. G. & KOMISSAROV, S. S. 1996 An upwind numerical scheme for relativistic hydrodynamics with a general equation of state. *Mon. Not. R. Astron. Soc.* **278** (2), 586–602.
- FAY, J. A. 1959 Two-dimensional gaseous detonations: velocity deficit. *Phys. Fluids* **2** (3), 283–289.
- GLASS, I. I. & LIU, W. S. 1978 Effects of hydrogen impurities on shock structure and stability in ionizing monatomic gases. Part 1. Argon. *J. Fluid Mech.* **84** (1), 55–77.
- GLAZ, H. M., COLELLA, P., GLASS, I. I. & DESCHAMBAULT, R. L. 1985a A detailed numerical, graphical, and experimental study of oblique shock wave reflections. *Tech. Rep.* LBL-20033. Lawrence Berkeley National Laboratory.
- GLAZ, H. M., COLELLA, P., GLASS, I. I. & DESCHAMBAULT, R. L. 1985b A numerical study of oblique shock-wave reflections with experimental comparisons. *Proc. R. Soc. Lond. A* **398** (1814), 117–140.
- GRIFFITHS, R. W., SANDEMAN, R. J. & HORNING, H. G. 1976 The stability of shock waves in ionizing and dissociating gases. *J. Phys. D: Appl. Phys.* **9** (12), 1681–1691.

- GRUN, J., STAMPER, J., MANKA, C., RESNICK, J., BURRIS, R., CRAWFORD, J. & RIPIN, B. H. 1991 Instability of Taylor–Sedov blast waves propagating through a uniform gas. *Phys. Rev. Lett.* **66** (21), 2738–2741.
- HENDERSON, L. F. & LOZZI, A. 1975 Experiments on transition of Mach reflexion. *J. Fluid Mech.* **68** (1), 139–155.
- HENDERSON, L. F., VASILEV, E. I., BEN-DOR, G. & ELPERIN, T. 2003 The wall-jetting effect in Mach reflection: theoretical consideration and numerical investigation. *J. Fluid Mech.* **479**, 259–286.
- HIGASHINO, F., HENDERSON, L. F. & SHIMIZU, F. 1991 Experiments on the interaction of a pair of cylindrical weak blast waves in air. *Shock Waves* **1** (4), 275–284.
- HORNUNG, H. 1985 The effect of viscosity on the Mach stem length in unsteady strong shock reflection. In *Flow of Real Fluids* (ed. G. E. A. Meier & F. Obermeier), pp. 82–91. Springer.
- HORNUNG, H. 1986 Regular and Mach reflection of shock waves. *Annu. Rev. Fluid Mech.* **18**, 33–58.
- HORNUNG, H. G. & LEMIEUX, P. 2001 Shock layer instability near the Newtonian limit of hypervelocity flows. *Phys. Fluids* **13** (8), 2394–2402.
- LAU-CHAPDELAIN, S. S. M. & RADULESCU, M. I. 2013 Non-uniqueness of solutions in asymptotically self-similar shock reflections. *Shock Waves* **23** (6), 595–602.
- LAU-CHAPDELAIN, S. S. M. & RADULESCU, M. I. 2016 Viscous solution of the triple-shock reflection problem. *Shock Waves* **26** (5), 551–560.
- LEE, J. H. S. 2008 *The Detonation Phenomenon*. Cambridge University Press.
- LI, H. & BEN-DOR, G. 1995 Reconsideration of pseudo-steady shock wave reflections and the transition criteria between them. *Shock waves* **5** (1–2), 59–73.
- LI, H. & BEN-DOR, G. 1999 Analysis of double-Mach-reflection wave configurations with convexly curved Mach stems. *Shock Waves* **9** (5), 319–326.
- MACH, P. 2011 Bifurcating mach shock reflections with application to detonation structure. Masters thesis, University of Ottawa.
- MACH, P. & RADULESCU, M. I. 2011 Mach reflection bifurcations as a mechanism of cell multiplication in gaseous detonations. *Proc. Combust. Inst.* **33** (2), 2279–2285.
- MALEY, L. 2015 On shock reflections in fast flames. Masters thesis, University of Ottawa.
- MALEY, L., BHATTACHARJEE, R., LAU-CHAPDELAIN, S. S.-M. & RADULESCU, M. I. 2015 Influence of hydrodynamic instabilities on the propagation mechanism of fast flames. *Proc. Combust. Inst.* **35** (2), 2117–2126.
- MISHIN, G. I., BEDIN, A. P., IUSHCHENKOVA, N. I., SKVORTSOV, G. E. & RIAZIN, A. P. 1981 Anomalous relaxation and instability of shock waves in gases. *Sov. Phys. Tech. Phys.* **26**, 2315–2324.
- MOEN, I. O., SULMISTRAS, A., THOMAS, G. O., BJERKETVEDT, D. & THIBAUT, P. A. 1986 Influence of cellular regularity on the behavior of gaseous detonations. In *Dynamics of Explosions* (ed. J. R. Bowen, J.-C. Leyer & R. I. Soloukhin), pp. 220–243.
- OHNISHI, N., SATO, Y., KIKUCHI, Y., OHTANI, K. & YASUE, K. 2015 Bow-shock instability induced by Helmholtz resonator-like feedback in slipstream. *Phys. Fluids* **27** (6), 066103.
- QUIRK, J. J. 1992 A contribution to the great Riemann solver debate. *ICASE Rep. No.* 92-94. Springer.
- RADULESCU, M. I. & LEE, J. H. S. 2002 The failure mechanism of gaseous detonations: experiments in porous wall tubes. *Combust. Flame* **131** (1), 29–46.
- RADULESCU, M. I., PAPI, A., QUIRK, J. J., MACH, P. & MAXWELL, B. M. 2009 The origin of shock bifurcations in cellular detonations. In *22nd International Colloquium on the Dynamics of Explosions and Reactive Systems*.
- RIKANATI, A., SADOT, O., BEN-DOR, G., SHVARTS, D., KURIBAYASHI, T. & TAKAYAMA, K. 2006 Shock-wave mach-reflection slip-stream instability: a secondary small-scale turbulent mixing phenomenon. *Phys. Rev. Lett.* **96** (17), 174503.
- RIKANATI, A., SADOT, O., BEN-DOR, G., SHVARTS, D., KURIBAYASHI, T. & TAKAYAMA, K. 2009 A secondary small-scale turbulent mixing phenomenon induced by shock-wave Mach-reflection slip-stream instability. In *Shock Waves* (ed. K. Hannemann & F. Seiler), vol. 2, pp. 1347–1352. Springer.
- SAMTANEY, R. & PULLIN, D. I. 1996 On initial-value and self-similar solutions of the compressible Euler equations. *Phys. Fluids* **8** (10), 2650–2655.

- SEMENOV, A. N., BEREZKINA, M. K. & KRASOVSKAYA, I. V. 2009a Classification of shock wave reflections from a wedge. Part 1. Boundaries and domains of existence for different types of reflections. *Tech. Phys.* **54** (4), 491–496.
- SEMENOV, A. N., BEREZKINA, M. K. & KRASOVSKAYA, I. V. 2009b Classification of shock wave reflections from a wedge. Part 2. Experimental and numerical simulations of different types of Mach reflections. *Tech. Phys.* **54** (4), 497–503.
- SEMENOV, A. N., BEREZKINA, M. K. & KRASSOVSKAYA, I. V. 2012 Classification of pseudo-steady shock wave reflection types. *Shock Waves* **22** (4), 307–316.
- SHARPE, G. J. & FALLE, S. A. E. G. 2011 Numerical simulations of premixed flame cellular instability for a simple chain-branching model. *Combust. Flame* **158** (5), 925–934.
- SHI, X., ZHU, Y., LUO, X. & YANG, J. 2017 Numerical study on double mach reflection of strong moving shock involving laminar transport. In *21st AIAA International Space Planes and Hypersonics Technologies Conference, Xiamen, China*.
- SHI, X., ZHU, Y., YANG, J. & LUO, X. 2019 Mach stem deformation in pseudo-steady shock wave reflections. *J. Fluid Mech.* **861**, 407–421.
- SIRMAS, N. & RADULESCU, M. I. 2015 Evolution and stability of shock waves in dissipative gases characterized by activated inelastic collisions. *Phys. Rev. E* **91** (2).
- SIRMAS, N. & RADULESCU, M. I. 2019 Structure and stability of shock waves in granular gases. *J. Fluid Mech.* **873**, 568–607.
- SKEWS, B. W. 1967 The shape of a diffracting shock wave. *J. Fluid Mech.* **29** (2), 297–304.
- SMITH, W. R. 1959 Mutual reflection of two shock waves of arbitrary strengths. *Phys. Fluids* **2** (5), 533–541.
- SORIN, R., ZITOUN, R., KHASAINOV, B. & DESBORDES, D. 2009 Detonation diffraction through different geometries. *Shock Waves* **19** (1), 11–23.
- STREHLOW, R. A. & BILLER, J. R. 1969 On the strength of transverse waves in gaseous detonations. *Combust. Flame* **13** (6), 577–582.
- URIBE, F. J. & VELASCO, R. M. 2018 Shock-wave structure based on the Navier–Stokes–Fourier equations. *Phys. Rev. E* **97** (4), 043117.
- VAN LEER, B. 1977 Towards the ultimate conservative difference scheme. IV. A new approach to numerical convection. *J. Comput. Phys.* **23** (3), 276–299.
- VASILEV, E. I., BEN-DOR, G., ELPERIN, T. & HENDERSON, L. F. 2004 The wall-jetting effect in Mach reflection: Navier–Stokes simulations. *J. Fluid Mech.* **511**, 363–379.
- VASILEV, E. I., ELPERIN, T. & BEN-DOR, G. 2008 Analytical reconsideration of the von Neumann paradox in the reflection of a shock wave over a wedge. *Phys. Fluids* **20** (4), 046101.